

# **Active control of an axisymmetric jet with distributed electromagnetic flap actuators**

**H. Suzuki, N. Kasagi, Y. Suzuki**

Hiroaki Suzuki  
Department of Mechanical Engineering, The University of Tokyo  
Hongo 7-3-1, Bunkyo-ku, Tokyo 113-8656, JAPAN  
hsuzuki@iis.u-tokyo.ac.jp

Nobuhide Kasagi  
kasagi@thtlab.t.u-tokyo.ac.jp

Yuji Suzuki  
ysuzuki@thtlab.t.u-tokyo.ac.jp

## **Abstract**

Miniature electromagnetic flap actuators are developed and mounted on the periphery of the nozzle exit of an axisymmetric jet to induce various flow modes and enhance mixing processes. It is demonstrated that the flap actuators can significantly modify the large-scale vortical structures. In particular, when the flaps are driven in anti-phase on either side of the jet, the jet bifurcates into two branches. Unlike the bifurcating jet reported by Lee and Reynolds (1985), the vorticity distribution along a vortex ring is uneven, causing an off-axis motion, and results in the jet bifurcation at a closer distance from the nozzle exit.

## **1**

### **Introduction**

Active control of the shear flow and associated momentum and scalar transport has been a central issue in modern scientific, engineering, and environmental research efforts (Moin and Bewley 1994, Gad-el-Hak 1996, Kasagi 1998). Since the large-scale coherent structures in turbulent shear flows play a primary role in the transport phenomena, selective manipulation of those structures is desired in order to achieve an efficient control (Cantwell 1981, Ho and Huerre 1984, Robinson 1991).

H. Suzuki et al., *Exp. Fluids* 36, 498-509 (2004)

In the meantime, micro-electro-mechanical systems (MEMS) technology has been developing rapidly, and now it is possible to fabricate solid-state micro sensors and actuators (Ho and Tai 1996, McMichael 1996, Ho and Tai 1998), which can be produced in large quantities through a batch fabrication process. With the micro devices, which offer a local and direct control input/output, even more efficient and flexible control of various shear flow phenomena became a realistic technological target (e.g., Liu et al. 1995, Jacobson and Reynolds 1998, Huang et al. 1998).

Among various shear flows, jets are used in a variety of industrial applications such as mixing, cooling/heating, drying, spraying, and printing. In this flow mode, the initial shear layer is extremely sensitive to small disturbances, which are amplified through their inherent instability (e.g., Huerre and Monkewitz 1990). As a result, large-scale vortical structures emerge at the frequency of disturbance.

Bulk forcing of a jet column has been often used to alter the vortex shedding, and much work has been made to investigate the mixing and entrainment properties (Winant and Browand 1974, Crow and Champagne 1971, Zaman and Hussain 1980, Gutmark and Ho 1983, Mankbadi 1992). More recently, non-axisymmetric control methods have also been attempted to achieve large alterations. Zaman et al. (1994) and Reeder and Samimy (1996) examined the effect of tab vortex generators placed inside the exit edge of a round jet nozzle. They found that each tab produced a pair of counter-rotating streamwise vortices, and that the entrainment of the ambient fluid was significantly enhanced with a relatively small thrust penalty. Longmire and Duong (1996) employed a round jet nozzle which had either stepped or sawtooth trailing edge, and showed that, when axial forcing at a low frequency was applied, a secondary jet was generated in the straining regions between primary ring cores at the fixed azimuthal location.

Active control strategies have also been pursued in order to achieve more drastic and flexible flow modifications. Corke and Kusek (1993) introduced localized acoustic disturbances, which were produced by an array of miniature loud speakers placed around the jet nozzle exit. They investigated the effect of the forcing of axisymmetric and counter-rotating helical modes in detail. Smith and Glezer (1997) successfully applied miniature zero-mass-flux jet actuators (synthetic jets) for the control of a large-scale planar jet. They showed that the primary jet could be vectored either toward or away from the synthetic jet actuators by creating low-pressure recirculating flow regions. Lee and Reynolds (1985) and Parekh et al. (1988) showed that it is possible

H. Suzuki et al., Exp. Fluids 36, 498-509 (2004)

to make a round jet bifurcate by imposing orbital and axial modes of forcing simultaneously. The requisite condition for the bifurcation is an orbital forcing frequency equal to twice the axial forcing frequency. Danaila and Boersma (2000) investigated the mechanism of a bifurcating jet with the aid of direct numerical simulation. They imposed an oscillating component, which consists of a pair of counter-rotating helical modes, on the nozzle exit velocity, and showed that the single-frequency excitation could trigger a bifurcating jet.

The fact that the small disturbance at the initial boundary layer can alter the entire jet flow field stimulated us to pursue a possibility of producing various jet flow modes with a single nozzle, utilizing distributed MEMS-based actuators, which can be driven independently according to a driving signal supplied by a control program. In most of the previous studies mentioned above, the control input mode introduced is limited to one or a few. Corke and Kusek (1993) studied the effect of the jet nozzle equipped with 12 miniature speakers mounted at the exit. However, their control modes used are only the helical modes of  $m = 0$  and  $m = \pm 1$ , where  $m$  denotes the azimuthal wave number.

The control strategy utilizing distributed miniature actuators has several advantages over the conventional bulk forcing scheme. Firstly, the mechanical disturbance can be introduced into the initial jet shear layer locally and directly, so that the large scale vortical structures can be produced with a smaller power input. Secondly, the control mode and frequency can be suitably selected and easily changed depending on the flow condition and the control target. Thus, it can be applied to various jet flows in wide engineering applications, where the flow condition may change over time.

For this purpose, miniature electromagnetic flap actuators are fabricated and mounted on the periphery of a round jet nozzle exit. The dynamics of coherent structures in the shear layer and their contribution to the global flow evolution are examined through flow visualization and quantitative velocity measurement. For the bifurcating jet, which exhibits the most drastic alteration, the spatio-temporal velocity and vorticity field are measured by using two-dimensional particle tracking velocimetry (hereafter, 2-D PTV). The physical model of the jet bifurcation mechanism is proposed based on both the flow visualization and the vorticity distribution measured. Finally, the comparison between the present bifurcation mechanism and previous studies is discussed.

## 2

### Experimental setup and procedure

#### 2.1

##### Electromagnetic flap actuator

Up to the present, various actuation principles (e.g., electrostatic, magnetic, thermal, chemical, piezoelectric, etc.) are proposed for the active flow control (Ho and Tai 1996, McMichael 1996, Ho and Tai 1998, Wilkinson 1989). However, none of them satisfies all requirements in the real applications, such as large force, rapid response, robustness in hostile environment, and small power consumption. For the present study, we employed the electromagnetic force, which can generate a large force over a large working distance. A major drawback of this type of actuators is its large power consumption.

Figure 1 shows the electromagnetic flap actuator ( $9 \times 3 \text{ mm}^2$ ) made of a copper plated polyimide film (Suzuki et al. 1999a, b). The polyimide and copper layer thicknesses are 25 and 35  $\mu\text{m}$ , respectively. A square copper coil is patterned lithographically and etched by ferric chloride solution. When the electric current is applied to the coil, the flap is elastically bent by the electromagnetic force between the coil and a cylindrical permanent magnet of 4000 Gauss placed underneath. At the root of the flap, a part of the polyimide film is hollowed with the laser machining system to reduce the bending stiffness.

The static displacement of the flap, which is measured at the center of the coil by a laser displacement meter (Keyence; LC-2440), is shown in Fig. 2. In this measurement, the position of the flap at rest is in contact with the top of the magnet; this is the same arrangement as the jet nozzle described later. The flap has an almost linear response to a DC input, and the displacement reaches about 0.4 mm at 1 A. Note that the gradient gradually decreases at a higher current due to the larger distance between the coil and the magnet.

Figure 3 shows the frequency response of the flap with an AC of 0.8 A in air and water. In this case, the flap is placed 1 mm above the magnet to keep the flap from hitting the top of the magnet. The first resonant frequency in air  $f_{ra}$  is 270 Hz with the amplitude of 0.8 mm. On the other hand, the resonant frequency is reduced to  $f_{rw} = 60 \text{ Hz}$  in water due to the added (virtual) mass effect. Note that, at the smaller frequencies ( $f_a < 10 \text{ Hz}$ ), the amplitude of the flap in both air and water is constant, and is almost the same as that of the static response shown in Fig. 2.

In jet experiments described later, square waves are employed as a driving signal, since they are found to give larger control effects than sinusoidal waves. Figure 4 shows the displacement of the flap in water when a  $\pm 1$ A square wave signal is applied at 3.3 Hz. Here, the initial position of the flap is in contact with the magnet, so that the negative displacement is prohibited. When the flap is repelled from the magnet, it firstly exhibits the damping oscillation at its natural frequency ( $f_{nw} = 74$  Hz in this case) for 4 to 5 periods, and then stabilizes at 0.32 mm. (Slight differences in the amplitude and natural frequency from Fig. 3 are simply due to the small variation in the dimensions of actuators fabricated.) Thus, the motion of the flap actuator follows the square-wave control signal almost exactly with no time delay at small driving frequencies.

In the following jet experiments, the driving frequency, which is set to around the preferred mode frequency of the jet, stays less than 10 Hz. Therefore, the flap response to the square wave signals is similar to Fig. 4. That is, the flap movement is accomplished with the minimum time delay.

## 2.2 Jet apparatus and measurement techniques

Figure 5(a) shows a perspective view of the axisymmetric nozzle (diameter  $D = 20$  mm) equipped with 18 electromagnetic flap actuators inside the nozzle exit. Cylindrical permanent magnets are embedded in the nozzle inside-wall. These flaps are placed at regular intervals and cover 86 % of the circumference. The neutral position of the flaps is in contact with the magnet, so that they can move only upward as illustrated in Fig. 5(b). Each flap is driven independently by the amplified electric current supplied by a multi-channel digital-analog board.

A schematic of the recirculating water tank facility is shown in Fig. 6(a). The jet nozzle has an area contraction ratio of 42 : 1 with an overall length of 150 mm, and is connected to a water tank ( $900 \times 800 \times 800$  mm<sup>3</sup>) horizontally. The interior wall profile of the nozzle contraction is fitted to a third-order polynomial. Water is driven by a magnetic pump into a 130 mm ID plenum, where a honeycomb and meshes are introduced. The Cartesian coordinate system is employed, in which  $x$  denotes the streamwise direction, while  $y$  and  $z$  denote the two perpendicular (vertical and horizontal) directions, respectively (Fig. 6b). The jet centerline exit velocity  $U_0$  is set to 150 mm/s, corresponding to  $Re_D = 3000$ , unless otherwise noted. The amplitude of the flap actuation is kept at 0.3 mm ( $0.02 D$ ) by adjusting the driving current.

H. Suzuki et al., Exp. Fluids 36, 498-509 (2004)

For the flow visualization of jet shear layer, the fluorescent dye (0.03 wt% Rhodamine B solution) is injected from a 0.5 mm wide annular slot fabricated inside the nozzle. Its volume flow rate is kept at 1.0 mL/s (0.02 % of the jet flow rate). A 25 mJ Nd:YAG pulsed laser (Newwave Research; Mini Lase II) or a stroboscope is employed for the illumination. For sectional views, a laser sheet is made through two cylindrical lenses. The visualized images are acquired by a 3 CCD camera (Sony; XC-003) and recorded onto a NTSC laser disk recorder (Sony; LVR-5000).

The spatio-temporal evolution of large-scale vortical structures is investigated with the aid of 2-D PTV. The particle images are acquired by a high-definition CCD camera (Sony XCH-1125;  $1920 \times 1024$  pixel<sup>2</sup>) through a window on the sidewall of the tank, and recorded on a high-definition laser disk recorder (Sony; HDL-5800) at 30 frame/s. For illumination of tracer particles, a Nd:YAG pulsed laser is employed to introduce a laser sheet of 1 mm in thickness vertically into the flow field. The frequency of the laser pulse is set at 60 Hz, so that two sets of particle images are obtained from one interlaced image. The flap driving signal and the laser pulse are synchronized with the TV signal. An analog image preprocessor (Nexus; VP-01) is employed to improve the signal-to-noise (S/N) ratio of the particle images. The acquired images are A/D converted by an image processor (Nexus; Nexus9000) and transferred to a workstation. Instantaneous velocity vectors are obtained by tracking each particle over three consecutive time steps. A binary cross-correlation method (Yamamoto et al. 1991) is employed to reject spurious vectors.

The flow is seeded with Nylon 12 spherical particles of a specific density of 1.02 and a diameter of 140 ~ 170  $\mu\text{m}$ . The seeding concentration is  $1.5 \times 10^{-4}$  g/cm<sup>3</sup>. The measurement area in the  $x$ - $y$  plane is  $110 \times 60$  mm<sup>2</sup> ( $5.5D \times 3D$ ). Phase-averaged velocity and vorticity field is calculated from 5600 instantaneous velocity fields in each sub-region of  $1.56 \times 1.56$  mm<sup>2</sup> ( $76 \times 40$  cells). The uncertainty interval of the instantaneous velocity measurement is estimated to be 1.5% of the jet centerline exit velocity at a 95% coverage.

Supplementary measurements are also made with a two-component fiber LDV (Dantec; 60X11), using two pairs of laser beams of 514.5 and 488 nm wavelengths from a 4W Ar ion laser. At each measurement station, statistics are computed from more than 15000 velocity samples at a sampling frequency on the order of 100 Hz, which is large enough to resolve the large scale structures.

### 3

## Results

### 3.1 Flow Visualization

A typical longitudinal sectional view of a natural jet is shown in Fig. 7(a). A laminar shear layer separates from the nozzle lip and rolls up into vortex rings at about  $x/D = 2.5$ . After experiencing some stages of coalescence, ring structures break down into three-dimensional turbulent puffs at  $x/D \sim 4$ .

Figure 7(b) shows the jet controlled by an axisymmetric flap motion (Axisymmetric Mode), in which all 18 flaps are driven in phase by a sinusoidal wave signal of  $f_a = 4$  Hz ( $St_a = f_a D/U_0 \sim 0.5$ ). The discrete axisymmetric vortex rings roll up at  $x/D \sim 2$  with a regular spacing, being synchronized with the flap motion. On the other hand, Fig. 7(c) shows the jet excited with a square wave signal, at the corresponding phase. In this case, the location of vortex roll-up moves upstream to  $x/D \sim 1.5$ . It is confirmed repeatedly that the vortex rings start to roll up closer to the nozzle exit with the square wave signal than the sinusoidal wave signal. Hereafter, Axisymmetric Mode refers an axisymmetric flap motion with a square wave signal.

Figure 8 shows the radial distributions of the streamwise mean velocity  $U$  and the root-mean-square streamwise velocity fluctuation  $u_{rms}$  measured by LDV at  $x/D = 0.25$ . The momentum thickness  $\theta$  is  $0.15D$ , which is much larger than that of conventional laboratory jets with a top-hat exit velocity profile. This is because the initial shear layer is disturbed by the flaps mounted inside the nozzle, which have a roughness effect even when they are at rest. The profiles of  $U$  are almost the same in both the natural jet and the excited jet with Axisymmetric Mode at  $St_a = 0.25$ . In the natural jet,  $u_{rms}$  is  $0.013 U_0$  and  $0.07 U_0$  at the centerline and in the shear layer, respectively. On the other hand, in the excited jet,  $u_{rms}$  is increased to  $0.19 U_0$  in the shear layer, while it is unchanged near the centerline. Therefore, unlike acoustic forcing, the disturbance presently generated by the flaps is introduced locally into the initial shear layer. Crow and Champagne (1971) reported that the flow downstream is insensitive to the amplitude of disturbance when it is more than  $0.02U_0$ . Thus, the amplitude of the flap presently employed should be large enough as an initial control input.

From the flow visualization image shown in Fig. 7, the vortex shedding seems to be locked in the forcing frequency. However, it turned out that, when the square wave signal is applied at the low frequency, two vortices are shed in one cycle; vortex rings are generated in both ascent and descent motions of the flap. Figure

H. Suzuki et al., Exp. Fluids 36, 498-509 (2004)

9 shows the phase-averaged velocities in the streamwise ( $\langle u \rangle$ ) and cross-stream ( $\langle v \rangle$ ) directions measured right downstream of the flaps ( $x/D = 0.25$  and  $r/D = 0.45$ ) when driven at 4 Hz ( $St_a \sim 0.5$ ). In the figure, the flaps are ascending at the phase of  $\phi = 0$ , while descending at  $\phi = \pi$ . The time lag of  $\pi$  exists between the nozzle exit and the measurement location, so that the phase  $\phi = 0$  corresponds to the instant when the effect of the flap descending motion has arrived. Similarly, the phase  $\phi = \pi$  corresponds to the instant when the effect of the flap ascending has arrived. The profile of  $\langle v \rangle / U_0$  shows that the shear layer fluctuates twice sharply (at  $\phi = 0.5\pi$  and  $1.5\pi$ ) due to both ascending and descending motion, when the square wave signal is applied (dotted line).

Note that the fluctuation accompanied with the descending motion is sharper ( $\phi = 0.5\pi$ ). Although the similar profile is observed when the sinusoidal wave is used, the amplitude of the fluctuation is smaller. In summary, at the very vicinity of the flaps, the strong velocity fluctuation occurs twice in one cycle of the square wave signal, corresponding to the ascending and descending motion of the flap. The fluctuation is more intense with the flap descending motion. When  $St_a$  is more than 0.3, the two undulations immediately merge at the vicinity of the nozzle, so that only the vortex shedding at the forcing frequency has been observed (Zaman and Hussain 1979). However, with  $St_a < 0.3$ , two vortex rings are observed visually during one cycle of the square signal.

Since the vortex shedding is locked in the flapping frequency or its subharmonics at the moderate Strouhal numbers ( $St_a < 1.0$ ), the vortex structures that has the non-uniform vorticity in the azimuthal direction are expected to emerge, when relative phases among the flaps are changed. To examine this fact, the effect of the helical mode excitation (see Corke and Kusek 1993) is tested, which is written as

$$A(t, \omega) = A_0 \sin(m\gamma - \omega t). \quad (1)$$

$A$ ,  $t$ ,  $\omega$ , and  $\gamma$  represent the amplitude, time, excitation frequency, and azimuthal angle, respectively. The  $m = 0$  excitation corresponds to the Axisymmetric Mode, which is already shown in Fig. 7(b). When  $m = 1$  excitation is applied, a continuous helical structure is generated. However, when the helical excitation of the higher azimuthal wave number ( $m \geq 2$ ) is applied, the change in the global behavior of the jet is not significant. The small variation of the resultant vortex structure is not clearly comprehended with the flow visualization because the sheet of the injected dye is already disturbed by the presence of the flaps.



Among various control modes examined, the most significant effect is observed when upper and lower halves of the 18 flaps are driven 180-degree out of phase (Alternate Mode; hereafter referred as AL); i.e., the flaps numbered  $i = 1 \sim 9$ , and  $i = 10 \sim 18$  (Fig. 6b) are driven by out-of-phase square signals (Fig. 10). Figure 11(a) shows a longitudinal sectional view of the AL controlled jet at  $f_a = 1.9$  Hz ( $St_a = 0.25$ ). The laser sheet is introduced into the plane including the flaps numbered  $i = 5$  and 14. In this case, the jet clearly bifurcates into two separate jets from  $x/D = 3$ . Figure 11(b) shows a close-up view illuminated by a stroboscope. Alternately inclined and bent vortex rings are shed at a frequency of  $2f_a$ . Therefore, two vortices are shed during one cycle of the flap motion. The marked difference from Axisymmetric Mode is that one half of the vortex is generated by the flap ascending (toward the jet centerline), while the other half is generated by the flap descending (toward the nozzle inside wall). Thus, the vortex rings generated by AL control mode have non-uniform vorticity distribution along its circumference. As the vortices are convected downstream, they are transported into two different directions from  $x/D \sim 3$  by their mutual interaction. It should be noted that, in the present AL control mode, the driving signal of the actuators should be a square wave in order to achieve intense vortical structures. When a sinusoidal wave signal is applied, the bifurcation effect is deteriorated.

In order to clarify the effect of  $St_a$  and  $Re_D$  on bifurcation, the centerline velocity at  $x/D = 6$  is measured by LDV. Since the location  $x/D \sim 6$  approximately corresponds to the end of the potential core in the natural jet, the mean velocity there is used to examine the bifurcation effect. Figure 12 shows the contours of the mean centerline velocity normalized by that of the natural jet at the same  $Re_D$ . The centerline velocity becomes the minimum at  $St_a = 0.25$ , regardless of the  $Re_D$  measured ( $2000 < Re_D < 13000$ ). This fact indicates that the bifurcating effect should be the maximum at this  $St_a$ . At the smaller  $Re_D$  ( $2000 < Re_D < 8000$ ), the reduction rate is more than 60 %, but it is gradually decreased as  $Re_D$  increases. It is conjectured that the displacement of the flaps becomes smaller with increasing the Reynolds number, since they suffer a larger fluid force because of the thinning of the boundary layer.

Figure 13 shows the flap driving signal for Rotary Alternate Mode, in which the plane of symmetry of the flap motion in Alternate Mode is rotated by 60 degrees at every actuation period. In this control mode, successive vortex rings are transported into six divergent directions. After they break down at  $x/D = 3$ , the dye spread more widely than that of the natural jet as shown in Fig. 14.

Figures 15 (a) ~ (c) show instantaneous cross-stream sections at  $x/D = 8$ . In the natural jet, the radial spreading extent of dye remains about  $2D$  in diameter (Fig. 15a). In the AL controlled jet (also see, Fig. 11), two blobs of dye are identified in the upper and lower part of Fig. 15 (b), indicating the bifurcation in the vertical direction. The diameter of each blob is almost the same as that of the natural jet. With Rotary Alternate Mode (Fig. 15c), dye spreads in all radial directions, so that the mixing should be significantly enhanced.

### 3.2.

#### Field measurement with 2-D PTV

The experimental condition of 2-D PTV measurement is summarized in Table 1. For the bifurcating jet with AL control, the measurement is performed in two perpendicular planes, i.e., in the plane of bifurcation ( $x$ - $y$  plane, bifurcating plane) and out of the plane ( $x$ - $z$  plane, bisecting plane).  $St_a$  for the AL mode is selected so that the optimum and its half and double frequencies are included. For the axisymmetric mode, the preferred mode of  $St_a = 0.3$  is selected.

Figures 16 (a) and (b) show the phase-averaged velocity fields over 180 flapping periods in AL controlled jet at  $St_a = 0.25$  in the bifurcating and bisecting planes, respectively. For clarity, only every other vector in each axis is plotted among all vectors obtained. Three blobs of alternately flipped jet core, centered at  $x/D = 2.5, 3.5$  and  $4.5$  (indicated by arrows), can be seen clearly in the bifurcating plane. On the other hand, the  $x$ -direction momentum decays and the ambient fluid is entrained toward the jet centerline at  $x/D = 3 \sim 4$  in the bisecting plane.

Figure 17 shows the cross-stream distributions of the streamwise mean velocity  $U$  at various axial locations. The velocity profiles near the nozzle exit ( $x/D = 0.5$ ) are almost identical in all cases. At  $x/D = 3$ , where the bifurcation takes place, the centerline velocity in the bifurcating jet is smaller than that in the natural jet. The profile becomes wider in the bifurcating plane, while it is narrower in the bisecting plane. At  $x/D = 5$ , the profile in the bifurcating plane clearly exhibits two separate peaks and a trough in between.

### 3.3.

#### Bifurcating mechanism in AL controlled jet

In this section, the bifurcating mechanism in AL controlled jet is discussed. Vortex formation and its motion at the vicinity of the nozzle exit are examined by flow visualization, and their evolution at  $x/D > 1$  is explored based on the vorticity field obtained by 2-D PTV measurement.

Figures 18(a)~(d) show successive flow visualization images close to the nozzle exit with AL mode control at  $St_a = 0.25$ . The relative phase of the flap motion is denoted by  $\phi$  ( $\pi$  corresponds to a half period). When  $\phi = 0$  (Fig. 18a), the flaps located on the lower half of the nozzle in the figure are ascending toward the jet centerline, while those on the upper half are moving toward the nozzle-inside wall. The dye concentration is seen right downstream of the nozzle exit, but no vortex can be identified at this time instant. When  $\phi = 0.27\pi$  (Fig. 18b), a vortex labeled A rolls up in the lower half of the nozzle, while the roll-up in the upper half (vortex labeled B) is delayed until  $\phi = 0.54\pi$  (Fig. 18c). Therefore, the vortex ring formed in AL control is initially inclined with respect to the nozzle axis. Moreover, since the convective velocity of vortex A is larger than that of vortex B (1.7 times larger at  $x/D = 0.9$ ), the vortex ring is further inclined and bent as it is convected downstream (Fig. 18d).

Figures 19 (a)~(d) show contours of phase-averaged vorticity at every  $\pi/2$  phase difference. The vorticity  $\langle \omega_z \rangle$  is normalized with  $U_0$  and  $D$ , where  $\langle \rangle$  denotes phase-averaged quantities. The uncertainty interval of normalized vorticity associated with the uncertainty of the phase-averaged velocity components is estimated to be less than 0.3 at 95% coverage. A pair of connected circles represent an inclined vortex ring, which also has been identified in the flow visualization. As shown in Fig. 18, inclined vortex rings roll up at  $x/D \sim 1$ . In Fig. 19(a), the upper half (B) generated by the flap descending motion has larger vorticity (marked as a larger circle) than the lower half (A) generated by the flap ascending motion (marked as a smaller circle). Note that the lower half (A) rolls up ahead of the upper half (B) as mentioned before.

This observation explains the difference of the convective velocity between the upper and lower halves of an inclined ring vortex shown in Fig. 18. The upper half vortex with larger vorticity (B) induces larger convective velocity onto the lower half with smaller vorticity (A). At the same time, the half vortex with larger vorticity located upstream (C) induces inward velocity (toward the jet axis) onto the half vortex (A), so that the vortex (A) is moved inward where the streamwise mean velocity is larger. As a result, the lower half (A) travels

H. Suzuki et al., Exp. Fluids 36, 498-509 (2004)

faster, and reaches to the preceding vortex (C) as shown in Fig. 19(b). As the interaction proceeds, the vortex (A) overtakes the vortex ring (C)-(D), and moves toward the off-axis direction (Fig. 19c). This alternate slip-through phenomenon is accomplished at around  $x/D = 3$ , and these vortical structures are gradually smeared out at farther downstream (Fig. 19d)

Figures 20 (a) ~ (c) show the behavior of jet core fluid at different flapping frequencies. In these figures, the jet core fluid is defined as the region of velocity magnitude  $\langle U_{abs} \rangle (\equiv \sqrt{\langle u \rangle^2 + \langle v \rangle^2}) > 0.85U_0$ , and shown as a shaded area with the vorticity contours. At  $St_a = 0.25$  (Fig. 20b; at the same phase as in Fig. 16a), the core fluid inside the inclined vortex rings is directed toward the off-axis direction, and the jet core fluid oscillates vigorously. This phenomenon results in the alternate flapping of the jet. The constrictions between the neighboring vortices correspond to the low speed regions where the ambient fluid is entrained.

At the lower  $St_a (= 0.125)$ , the streamwise spacing of the successive vortex rings becomes much larger as shown in Fig. 20(a). Hence, the induced velocity between successive vortex rings should become much smaller, since the velocity induction based on the Biot-Savart law is inversely proportional to the square of the distance from the vortex core. Although the initial inclination of the vortex rings is larger, the slip-through motion of half vortices does not take place, and the jet core oscillates less vigorously.

At the higher  $St_a (= 0.5, \text{ Fig. 20c})$ , the successive vortex rings are closely spaced, so that the half vortex having smaller circulation mentioned in the previous figures is engulfed by the preceding half vortex with the larger vorticity, in the vicinity of the nozzle exit. Hence, the strong vortices generated by the flap descending line up in a staggered arrangement at a regular spacing, and only small undulation of the potential core is observed. The slip-through phenomenon does not occur, because the convective velocity as well as the vorticity of each vortex is all the same due to the same vorticity magnitude. Therefore, the jet core does not oscillate either.

A possible scenario of the bifurcation mechanism derived from the present results is schematically given in Fig. 21. The phase of this diagram corresponds to that of Fig. 19 (c). With AL mode control, a vortex ring with different magnitude of vorticity between upper and lower halves rolls up; the stronger half is generated by

H. Suzuki et al., Exp. Fluids 36, 498-509 (2004)

the flap descending, and the weaker half is generated by the flap ascending. As the weaker half is convected faster than the stronger half and approaches the stronger half of the preceding vortex ring, it overtakes the preceding vortex ring. Due to their mutual interaction, both halves are directed toward the off-axis directions. Consequently, the vortex rings are strongly inclined, and induce the alternate off-axis velocity onto the jet core fluid.

## 4

### COMPARISON WITH THE PREVIOUS STUDIES

In this chapter, the bifurcation mechanism in the present study is compared with that of bifurcating jets previously reported. According to Parekh et al. (1988), a bifurcating jet is defined as a jet splitting into two separate branches, and/or having a velocity profile with two distinct peaks. In the previous studies, it has been achieved mostly by a combination of an axial and an azimuthal forcing at the moderate Reynolds number, yet an azimuthal forcing can be either passive or active (Lee and Reynolds 1985, Parekh et al. 1988, Longmire and Duong 1996).

Recently, Danaila and Boersma (2000) performed a direct numerical simulation (DNS) of an axisymmetric jet flow with time-varying initial velocity profile. They primarily investigated two types of excitation, which are referred as flapping (F) excitation (containing the helical  $m = \pm 1$  modes with the same frequency and amplitude) and bifurcating (BF) excitation (superposition of the axisymmetric  $m = 0$  mode on the flapping mode with the same amplitude, but subharmonic frequency). The (BF) excitation is employed as a direct analogy to the experiment done by Lee and Reynolds (1985) and Parekh et al. (1988). They found that the jet splits into two branches when (F) excitation is applied. However, with (BF) excitation, the jet splits into  $\Psi$  shaped branches, which was different from the experimental observations. They conjecture that it is because, in the Lee and Reynolds' experiment, the axial and radial excitations are decoupled in each direction, while their (BF) excitation only involves the variation in the axial direction.

The excitation scheme in the present study is similar to (F) excitation, which utilizes single frequency mode excitation with a phase difference. However, since we employ a square wave signal, the formation mechanism of the tilted vortices is different. Danaila and Boersma (2000) employed a sinusoidal wave as an

H. Suzuki et al., Exp. Fluids 36, 498-509 (2004)

excitation signal, so that primary vortices roll up due to the instability at  $x/D \sim 2$  (e.g., see Fig. 1 of Danaila and Boersma 2000). In the present study, intense vortex rings are formed immediately at the nozzle exit. It is accomplished due to the step-like motion of the flap. Then, inhomogeneous distribution of vorticity magnitude between the upper and lower halves makes the convection velocity different, and the vortices are inclined at much larger angle as they go downstream. As a result, the interaction between neighboring vortices is more intense and starts at a closer distance from the nozzle exit, so that the bifurcation also occurs within a shorter distance.

Figure 22 shows the profiles of the axial mean velocity in the present study ( $St_a = 0.25$  and  $u_{rms}/U = 0.2$ ), Lee and Reynolds ( $St_a = 0.46$  and  $A_a = 0.17$ ), and Danaila and Boersma ( $St_{\pm 1} = 0.55$  and  $A_{\pm 1} = 0.15$ ) at  $x/D = 3, 4, 5$ , and  $6.5$ . The excitation frequency in the present study is approximately half of the others, since two vortices are shed in one period of the square signal. For Danaila and Boersma (2000), since the profiles at the same locations are not given, profiles at closer locations are shown ( $x/D = 3.1, 4.15, 5.2$  and  $6.25$ ). The experimental profiles of Lee and Reynolds are in good agreement with the simulation of Danaila and Boersma at  $x/D < 5$ . The two separate peaks in their velocity profile appear at  $x/D > 6$ , while Lee and Reynolds show much more marked trough in between. On the other hand, due to the formation of the inclined vortices closer to the nozzle exit, the profiles obtained in the present study are more widely spread at a closer distance to the nozzle exit; the distinct peaks in the velocity profile appear at around  $x/D = 5$ .

## 5

### CONCLUDING REMARKS

A novel axisymmetric jet nozzle equipped with a row of miniature flap actuators on its exit lip has been developed. The electromagnetic flap actuator is designed and fabricated through photolithography of a copper plated polyimide film. Its static and dynamic response in both air and liquid environment is characterized. The behavior of the controlled jet flow is examined through flow visualization and 2-D PTV measurement. It is found that the coherent vortical structures are shed being phase-locked to the flap movement and hence the flow field is modified significantly. In particular, when the flaps on either side of the jet are driven in anti-phase

H. Suzuki et al., Exp. Fluids 36, 498-509 (2004)

(Alternate Mode), the jet bifurcates into two separate jets without any bulk flow forcing. The most effective flapping Strouhal number is found to be  $St_a = 0.25$  for  $Re_D < 13000$ .

It is found that alternately inclined and bent vortex rings are formed near the nozzle exit. As they are convected downstream, they induce overtaking motion and turn away from the original jet axis. On the basis of the present results, a conceptual model of the bifurcating jet is presented. It is suggested that both the difference of the vorticity magnitude between the upper and lower halves of the vortex ring and that of their convective velocities should be responsible for the jet bifurcation. The bifurcation mechanism in the present study has many aspects in common with that of Lee and Reynolds (1985), Parekh et al. (1988), and Danaila and Boersma (2000), e.g., the mutual induction between vortex rings is responsible for the jet bifurcation. It is also supported by the fact that the optimum vortex shedding frequencies are almost the same ( $St \sim 0.5$ ). However, the inclined angle and intensity of vortex rings are larger due to the step-like motion of the flaps, so that the overtaking phenomenon of vortex rings occurs. Therefore, the bifurcation takes place at a shorter distance from the nozzle exit.

## Acknowledgements

The authors gratefully acknowledge Professors H. Miura and I. Shimoyama for their guidance in developing the actuators. We would like to thank Mr. N. Kurimoto for his help in the flap characterization. This work was supported through the Grant-in-Aid for Scientific Research (No. 10355010) by the Ministry of Education, Culture, Sports, Science, and Technology.

## References

- Cantwell BJ** (1981) Organized motion in turbulent flow. Ann. Rev. Fluid Mech. 13: 457-515
- Corke TC; Kusek SM** (1993) Resonance in axisymmetric jets with controlled helical-mode input. J. Fluid Mech. 249: 307-336
- Crow SC; Champagne FH** (1971) Orderly structure in jet turbulence. J. Fluid Mech. 48: 547-591
- Danaila I; Boersma BJ** (2000) Direct numerical simulation of bifurcating jets. Phys. Fluids 12: 1255-1257

H. Suzuki et al., *Exp. Fluids* 36, 498-509 (2004)

**Freund JB; Moin P** (2000) Jet mixing enhancement by high-amplitude fluidic actuation. *AIAA J.* 38: 1863-1870

**Gad-el-Hak M** (1996) Modern developments in flow control. *Appl. Mech. Rev.* 49: 365-379

**Gutmark E; Ho CM** (1983) Preferred modes and the spreading rates of jets. *Phys. Fluids* 26: 2932-2938

**Ho CM; Huerre P** (1984) Perturbed free shear layers. *Ann. Rev. Fluid Mech.* 16: 365-424

**Ho CM; Tai YC** (1996) Review: MEMS and its applications for flow control. *ASME J. Fluids Eng.* 118: 437-447

**Ho CM; Tai YC** (1998) Micro-Electro-Mechanical-Systems (MEMS) and fluid flows. *Ann. Rev. Fluid Mech.* 30: 579-612

**Huang C; Najafi K; Alnajjar E; Christophorou C; Naguib A; Nagib HM** (1998) Operation and testing of electrostatic microactuators and micromachined sound detectors for active control of high speed flows. *Proc. 11th IEEE MEMS Workshop, Heidelberg*: 81-86

**Huerre P; Monkewitz PA** (1990) Local and global instabilities in spatially developing flows. *Ann. Rev. Fluid Mech.* 22: 473-537

**Jacobson SA; Reynolds WC** (1998) Active control of streamwise vortices and streaks in boundary layers. *J. Fluid Mech.* 360: 179-211

**Kasagi N** (1998) Progress in direct numerical simulation of turbulent transport and its control. *Int. J. Heat & Fluid Flow* 19: 128-134

**Lee M; Reynolds WC** (1985) Bifurcating and blooming jets. Report TF-22, Thermosciences Division, Dept. of Mech. Eng., Stanford University

**Liu C; Tsao T; Tai YC** (1995) Out-of-plane permalloy magnetic actuators for delta-wing control. *Proc. 8th IEEE MEMS Workshop, Amsterdam*: 7-12

**Longmire EK; Duong LH** (1996) Bifurcating jets generated with stepped and sawtooth nozzles. *Phys. Fluids* 8: 978-992

**Mankbadi RR** (1992) Dynamics and control of coherent structure in turbulent jets. *Appl. Mech. Rev.* 45: 219-247

**McMichael JM** (1996) Progress and prospects for active flow control using microfabricated electromechanical systems (MEMS). *AIAA Paper 96-0306*

**Moin P; Bewley T** (1994) Feedback control of turbulence. *Appl. Mech. Rev.* 47 (6): S3-S13

**Parekh DE; Leonard A; Reynolds WC** (1988) Bifurcating jets at high Reynolds numbers. Report TF-35, Thermosciences Division, Dept. of Mech. Eng., Stanford University

**Reeder MF; Samimy M** (1996) The evolution of a jet with vortex generating tabs: real-time visualization and quantitative measurements. *J. Fluid Mech.* 311: 73-118

**Robinson SK** (1991) Coherent motions in the turbulent boundary layer. *Ann. Rev. Fluid Mech.* 23: 601-639



H. Suzuki et al., Exp. Fluids 36, 498-509 (2004)

**Smith BL; Glezer A** (1997) Vectoring and small scale motions effected in free shear flows using synthetic jet actuators. AIAA-paper 97-0213

**Suzuki H; Kasagi N; Suzuki Y; Shima H** (1999a) Manipulation of a round jet with electromagnetic flap actuators. Proc. 12th IEEE MEMS Conference, Orlando: 534-540

**Suzuki H; Kasagi N; Suzuki Y** (1999b) Active Control of an Axisymmetric Jet with an Intelligent Nozzle. Proc. 1st Symp. Turbulent Shear Flow Phenomema, Santa Barbara: 665-670

**Wilkinson SP** (1989) Interactive wall turbulence control: Viscous drag reduction in boundary layers, D. M. Bushnell and J. N. Hefner, eds., Prog. Astro. and Aero.: 123: 479

**Winant CD; Browand FK** (1974) Vortex pairing: the mechanism of mixing layer growth at moderate Reynolds number. J. Fluid Mech. 63: 237-255

**Yamamoto F; Uemura T; Iguchi T; Morita Z** (1991) A binary correlation method using a proximity function for 2-D and 3-D PTV. Exp. Numerical Flow Vis., Khalighi, B., et al., eds., New York, ASME: 23

**Zaman KBMQ; and Hussain AKMF** (1980) Vortex pairing in a circular jet under controlled excitation. Part 1. General jet response. J. Fluid Mech. 101: 449-491

**Zaman KBMQ; Reeder MF; Samimy M** (1994) Control of an axisymmetric jet using vortex generators. Phys. Fluids 6: 778-793

## List of Tables and Figures:

Table 1 Experimental condition for 2-D PTV measurement.

Fig. 1 Overview of an electromagnetic flap actuator and (b) the schematic diagram.

Fig. 2 Static response of the flap actuator.

Fig. 3 Dynamic response of the flap actuator. The scale of the horizontal axis is changed at 10Hz for clarity.

Fig. 4 Flap response to a square-wave control signal.

Fig. 5 (a) A perspective view of the jet nozzle equipped with 18 flap actuators. (b) Installation of the flap actuator.

Fig. 6 Experimental facilities. (a) Recirculating water tank, and (b) arrangement of flap actuators on the nozzle exit.

Fig. 7 Longitudinal sectional views of the jet shear layer: (a) natural jet, (b) Axisymmetric Mode with sinusoidal wave signal at  $St_a = 0.5$ , (c) Axisymmetric Mode with square wave signal at  $St_a = 0.5$

Fig. 8 Cross-stream distributions of streamwise mean and rms velocity at the nozzle exit.

Fig. 9 Phase-averaged velocities at  $x/D = 0.25$  and  $r/D = 0.45$  when flaps are driven by sinusoidal and square waves.

Fig. 10 Control signal diagram of Alternate Mode.

Fig. 11 Bifurcating jet excited with Alternate Mode at  $St_a = 0.25$ ; (a) Longitudinal sectional view, (b) Close-up view.

Fig. 12 Relative centerline velocity of the AL controlled jet at various flapping frequencies.

Fig. 13 Control signal diagram of Rotary Alternate Mode.

Fig. 14 Longitudinal sectional view of Rotary Alternate Mode.

Fig. 15 Transverse sectional views at  $x/D = 8$ , (a) Natural jet, (b) Alternate Mode, (c) Rotary Alternate Mode.

Fig. 16 Phase-averaged velocity vectors for Alternate Mode at  $St_a = 0.25$ ; (a) Bifurcating plane, (b) Bisecting plane.

Fig. 17 Cross-stream distributions of streamwise mean velocity.

Fig. 18 Successive flow visualization images near the nozzle exit for Alternate Mode at  $St_a = 0.25$ .

Fig. 19 Successive vorticity contours for Alternate Mode at  $St_a = 0.25$ .

Fig. 20 Jet core ( $\langle U_{abs} \rangle > 0.85U_0$ , shaded area) and vorticity contours at  $St_a =$  (a) 0.125, (b) 0.25, and (c) 0.5.

Fig. 21 Proposed model of vortex structures and their motion in the bifurcating jet generated with Alternate Mode.

H. Suzuki et al., Exp. Fluids 36, 498-509 (2004)

Fig. 22 Comparison of cross-stream distributions of streamwise mean velocity in the bifurcating planes. The solid line represents the present study ( $x/D = 3, 4, \text{ and } 5$ ). The circle data symbols represent data from Lee and Reynolds ( $x/D = 3, 4, 5, \text{ and } 6.5$ ). The broken line represents data from Danaila and Boersma ( $x/D = 3.1, 4.15, 5.2, \text{ and } 6.25$ ).

Table 1 Experimental condition for 2-D PTV measurement.

Control Mode	Flap-motion Strouhal Number ( $St_a$ )
Natural Jet	-
Alternate Mode (Bifurcating Plane)	0.125, 0.25, 0.5
Alternate Mode (Bisecting Plane)	0.25
Axisymmetric Mode	0.3

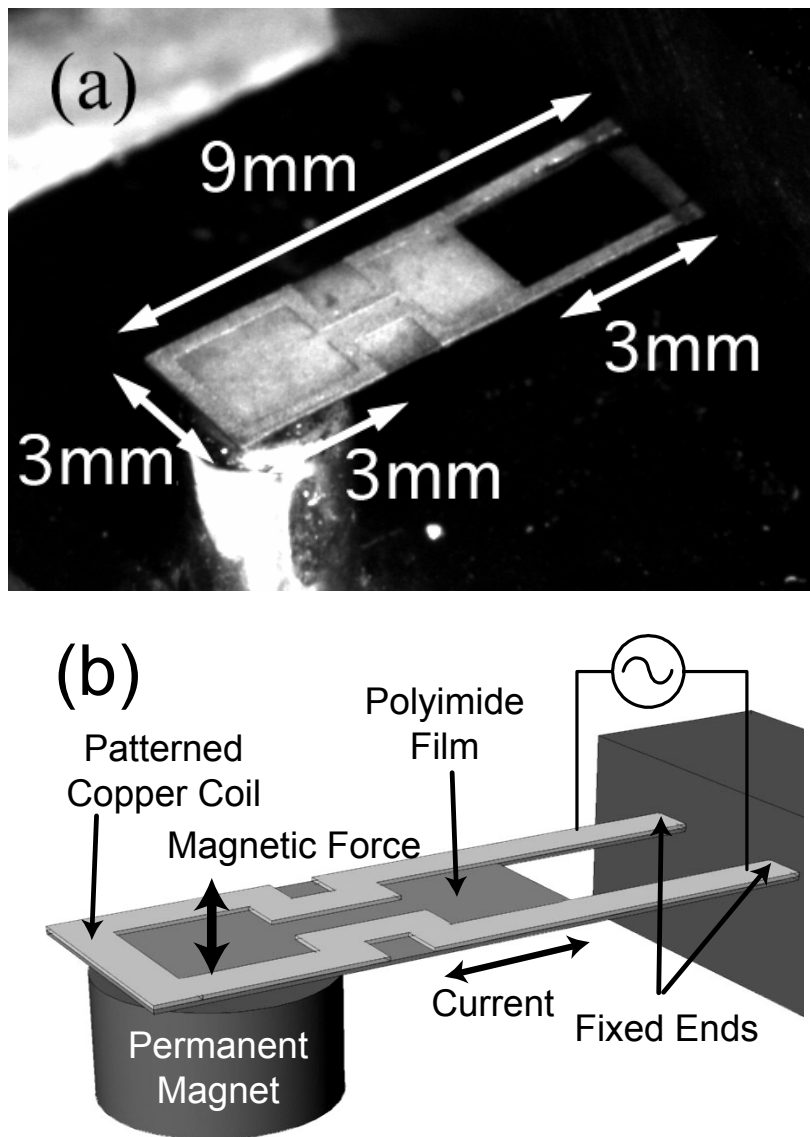


Fig. 1 (a) Overview of an electromagnetic flap actuator and (b) the schematic diagram.

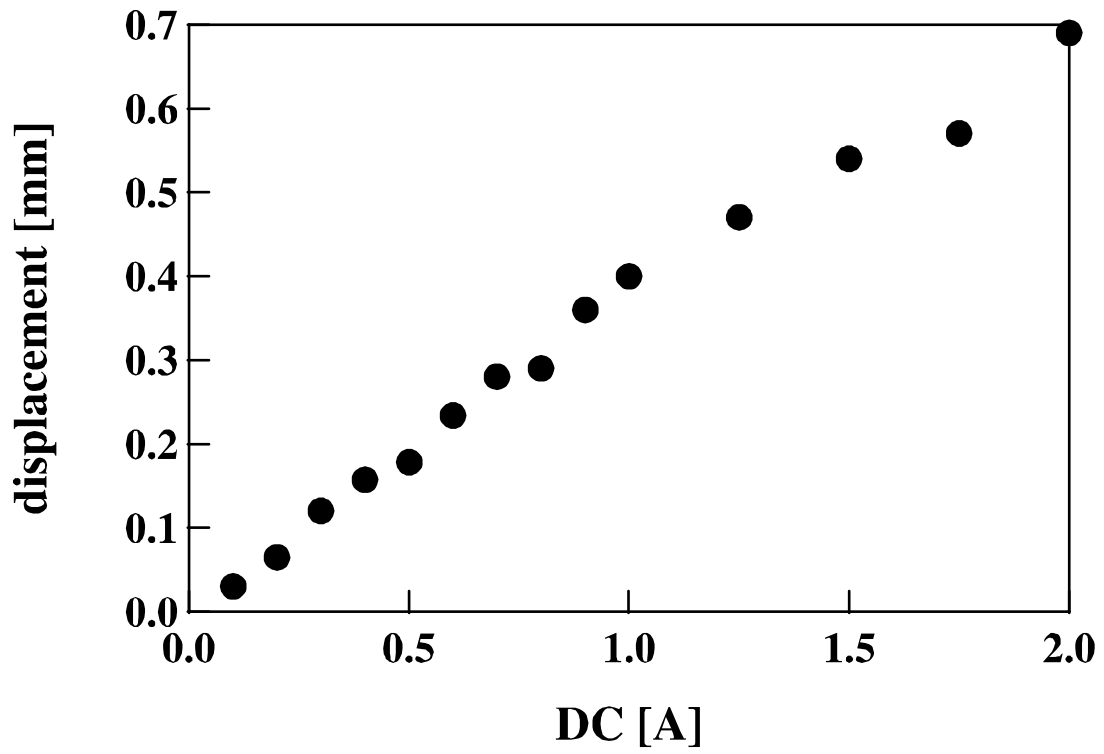


Fig. 2 Static response of the flap actuator.

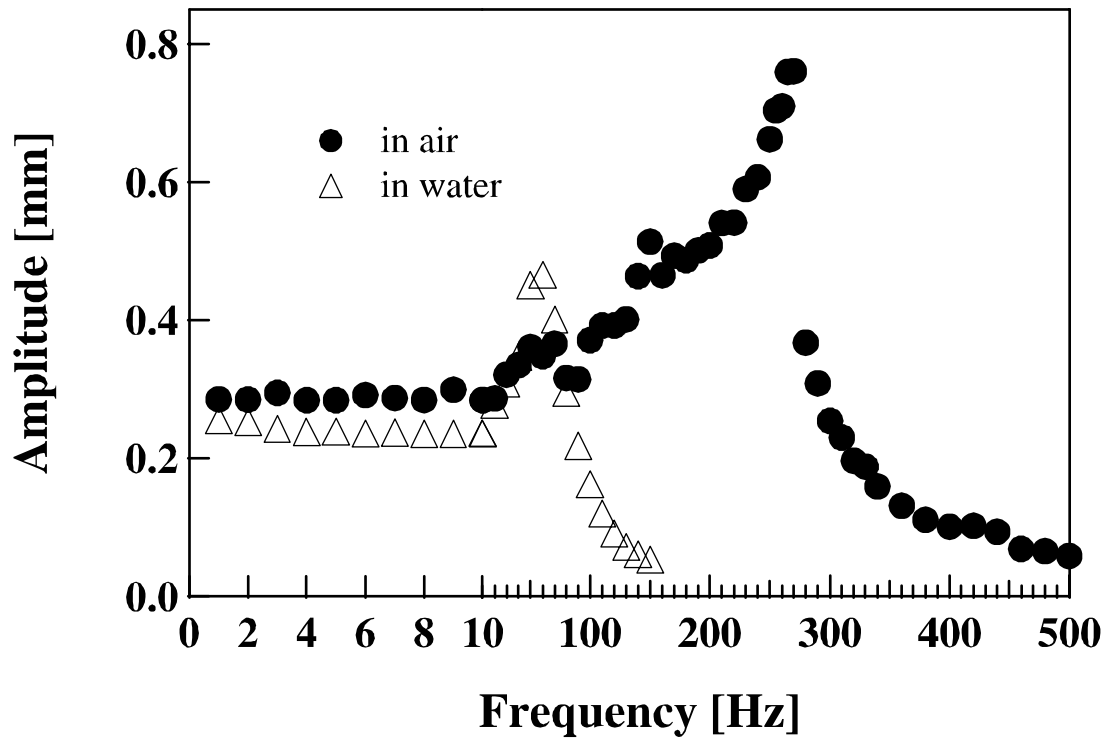


Fig. 3 Dynamic response of the flap actuator. The scale of the horizontal axis is changed at 10Hz for clarity.

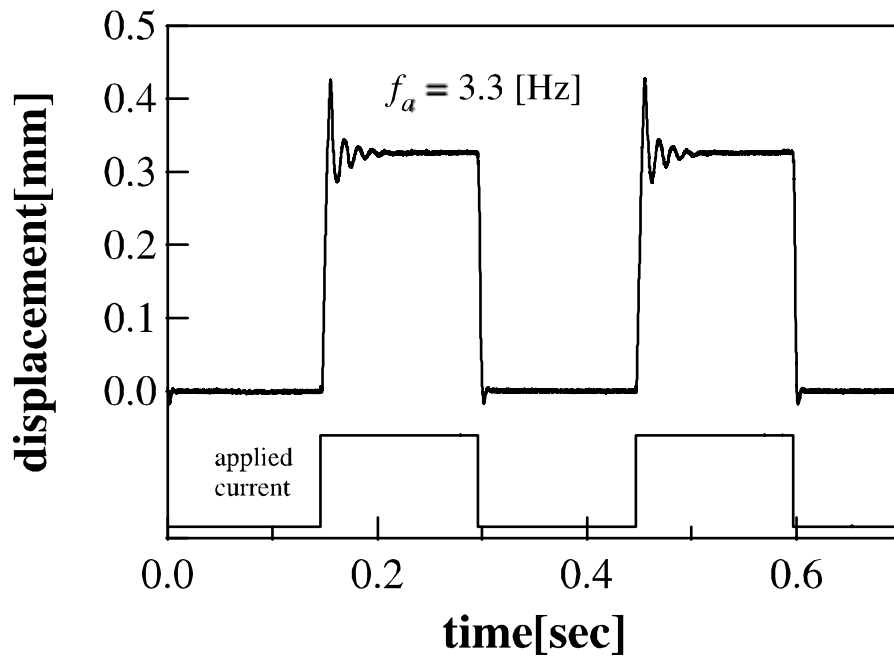
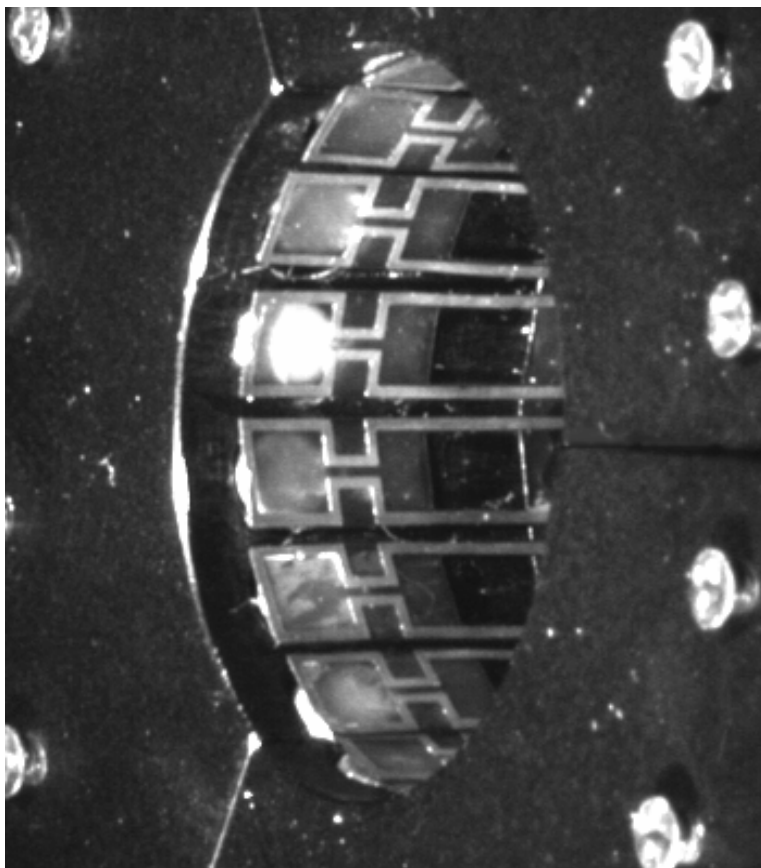


Fig. 4 Flap response to a square-wave control signal.



(a)



(b)

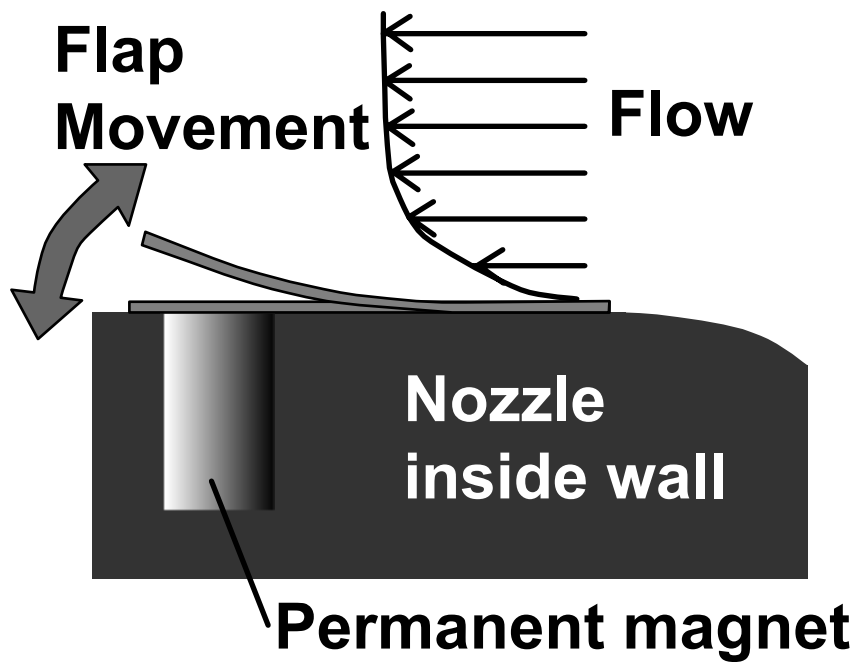
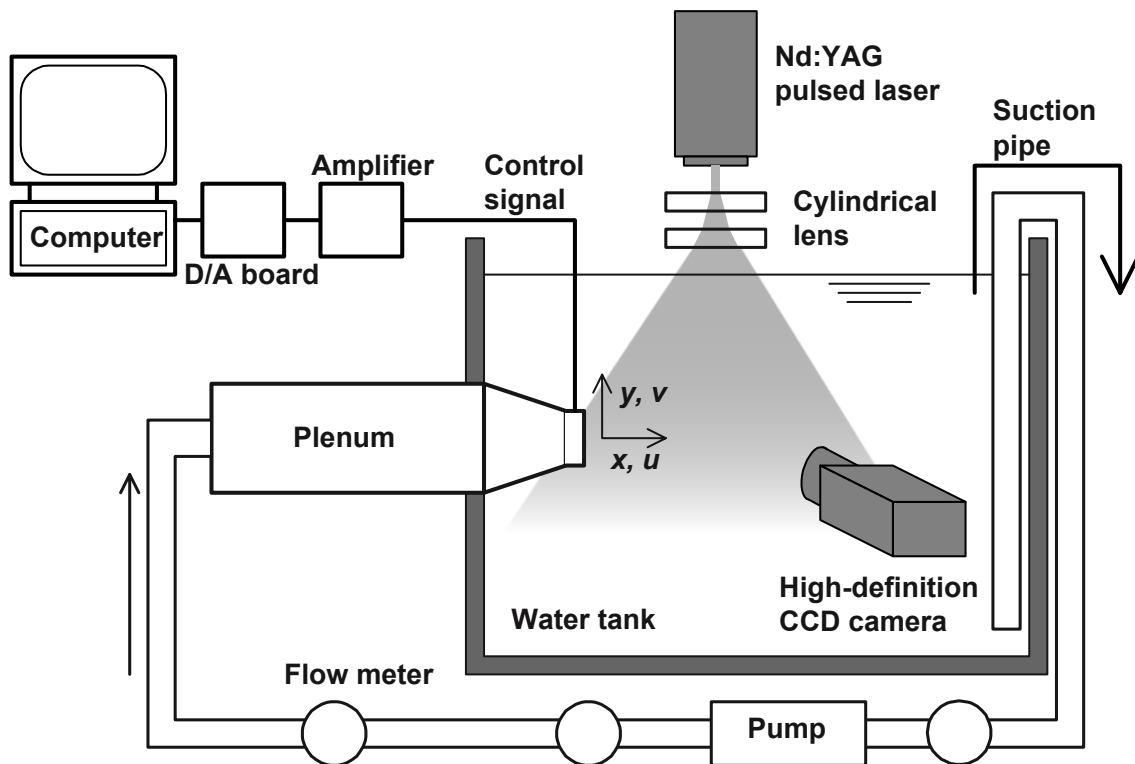


Fig. 5 (a) A perspective view of the jet nozzle equipped with 18 flap actuators. (b) Installation of the flap actuator.

(a)



(b)

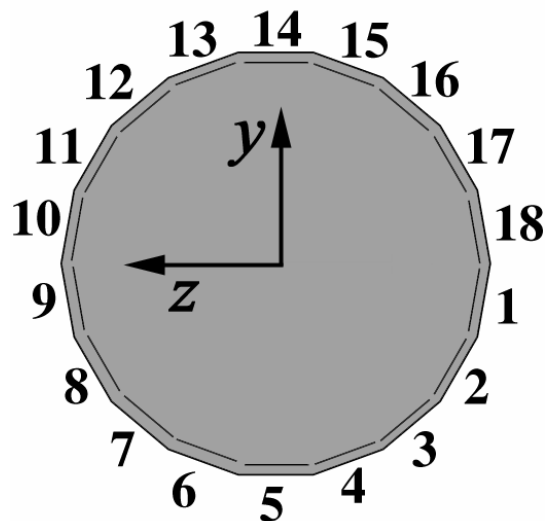
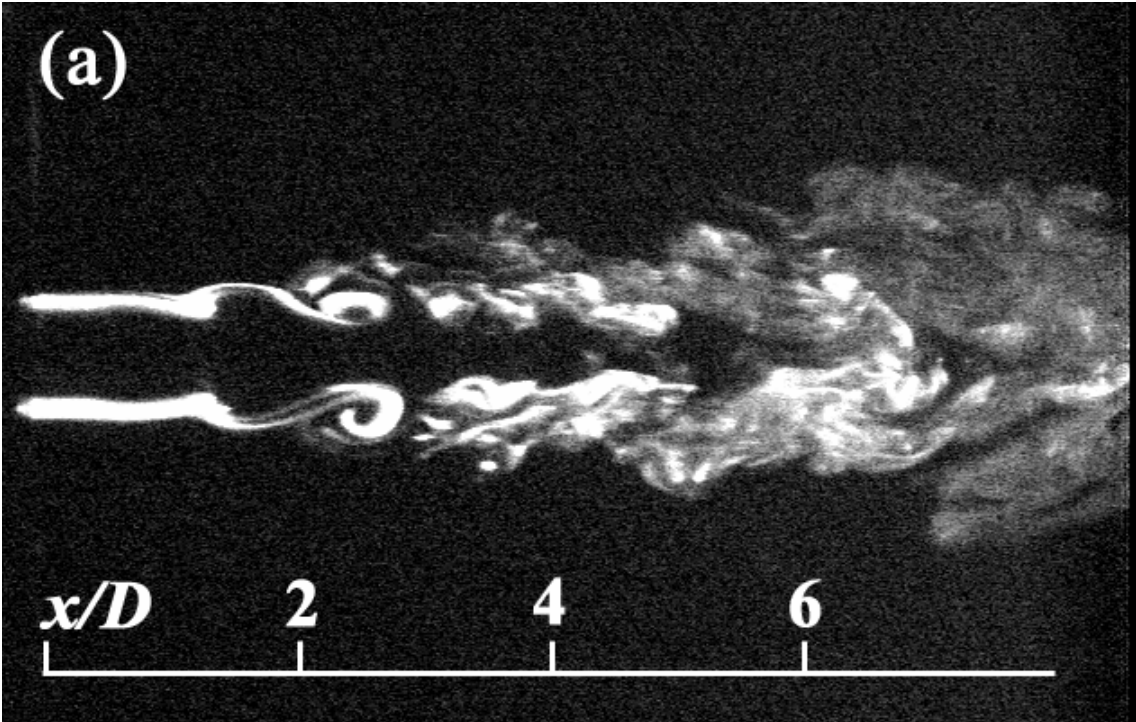


Fig. 6 Experimental facilities. (a) Recirculating water tank, and (b) arrangement of flap actuators on the nozzle exit.



[Fig. 7(a)]

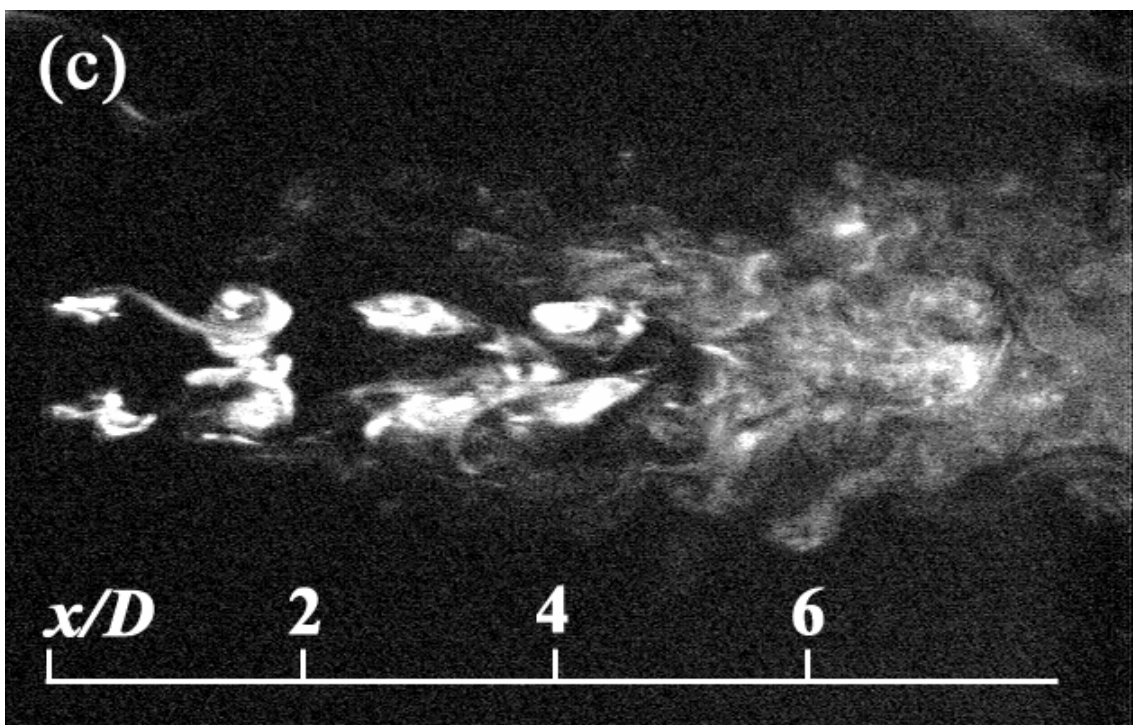
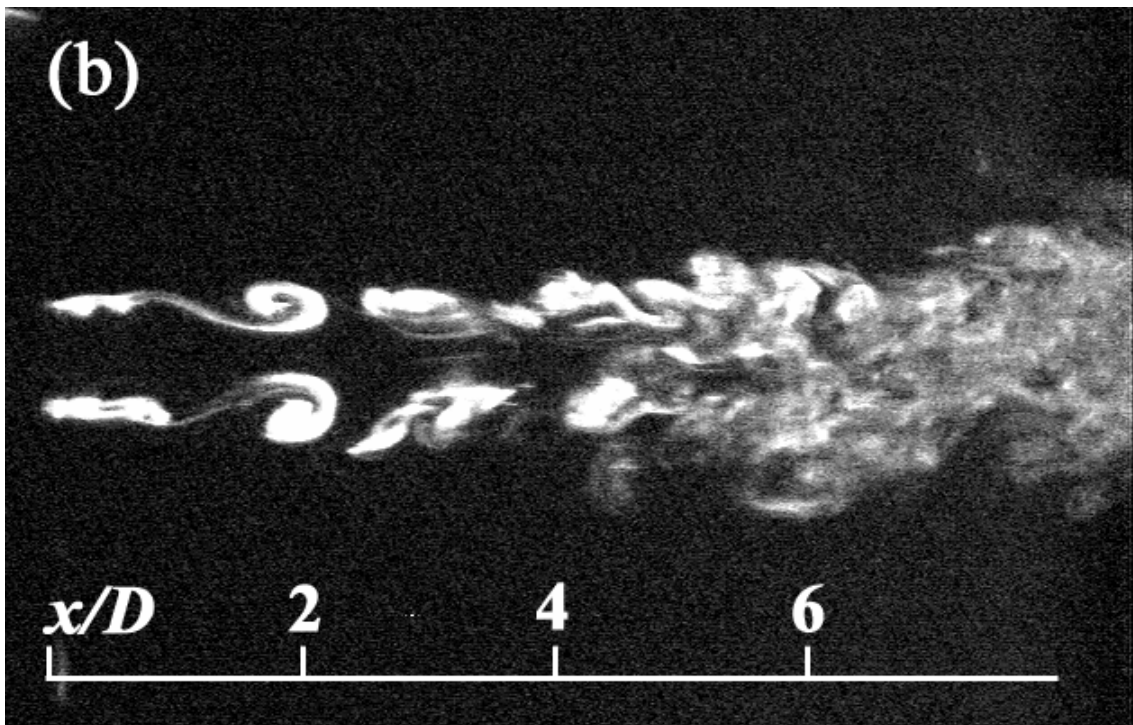


Fig. 7 Longitudinal sectional views of the jet shear layer: (a) natural jet, (b) Axisymmetric Mode with sinusoidal wave signal at  $St_a = 0.5$ , (c) Axisymmetric Mode with square wave signal at  $St_a = 0.5$ .

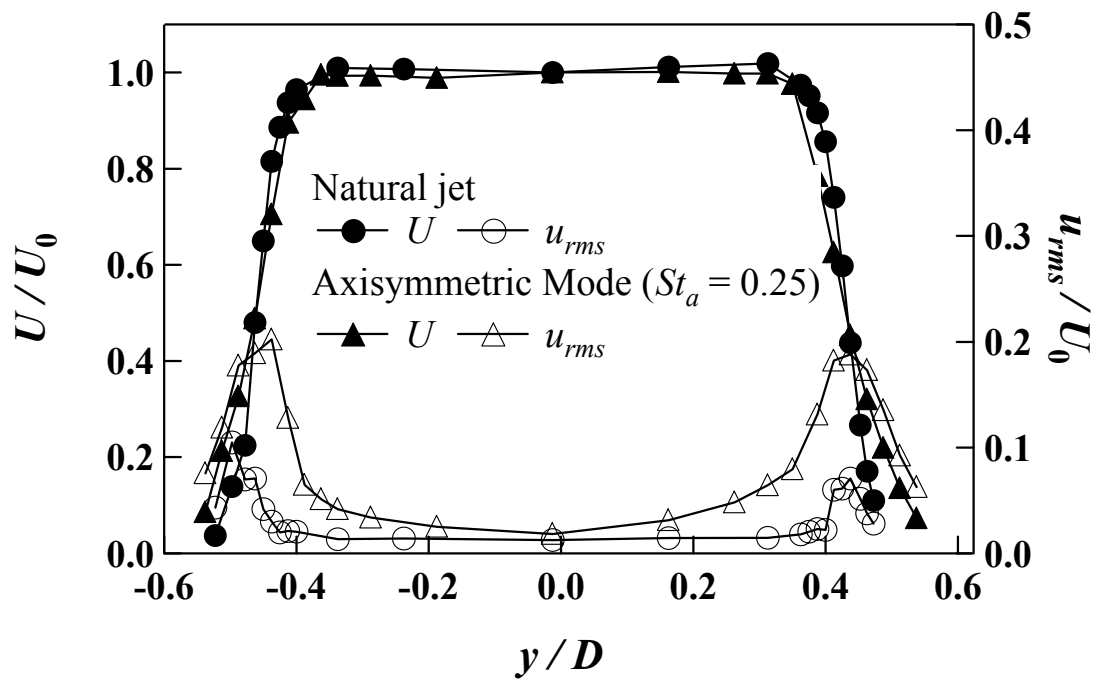


Fig. 8 Cross-stream distributions of streamwise mean and rms velocity at the nozzle exit.

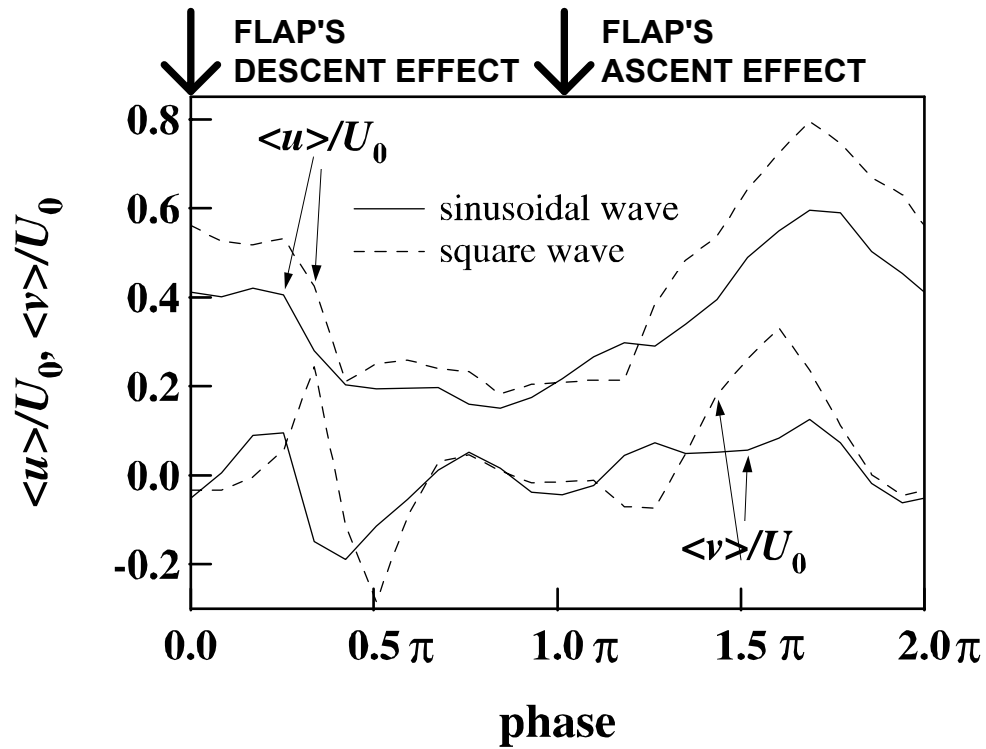


Fig. 9 Phase-averaged velocities at  $x/D = 0.25$  and  $r/D = 0.45$  when flaps are driven by sinusoidal and square waves.

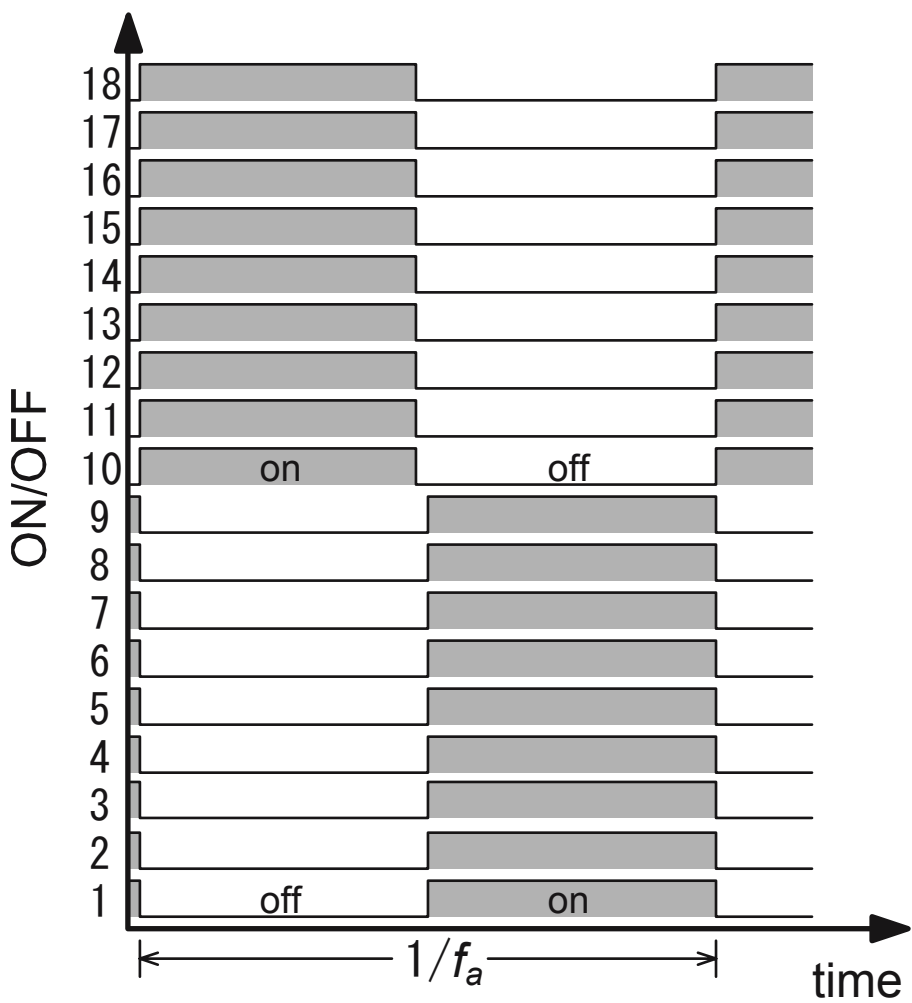


Fig. 10 Control signal diagram of Alternate Mode.

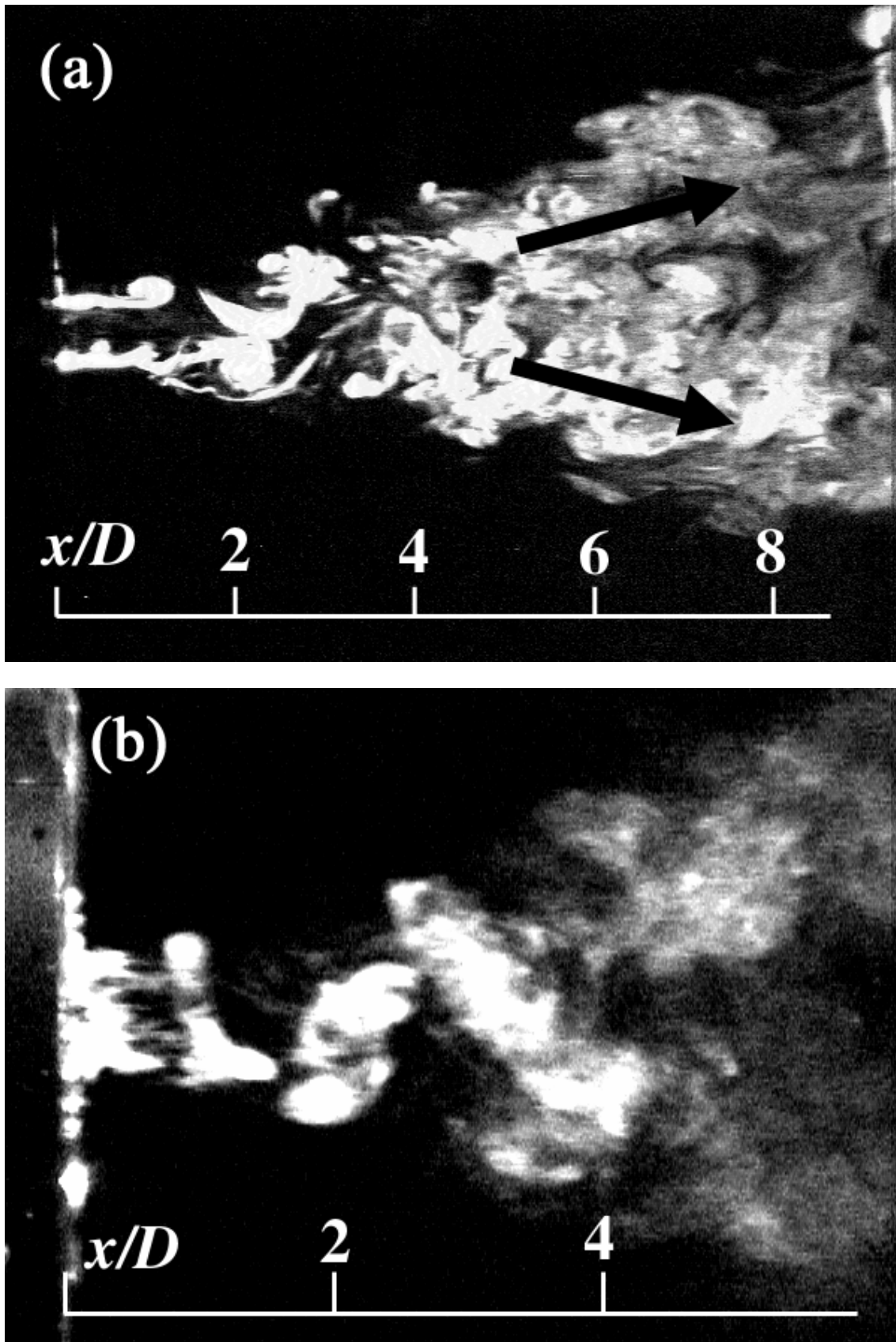


Fig. 11 Bifurcating jet excited with Alternate Mode at  $St_a=0.25$ ; (a) Longitudinal sectional view, (b) Close-up view.



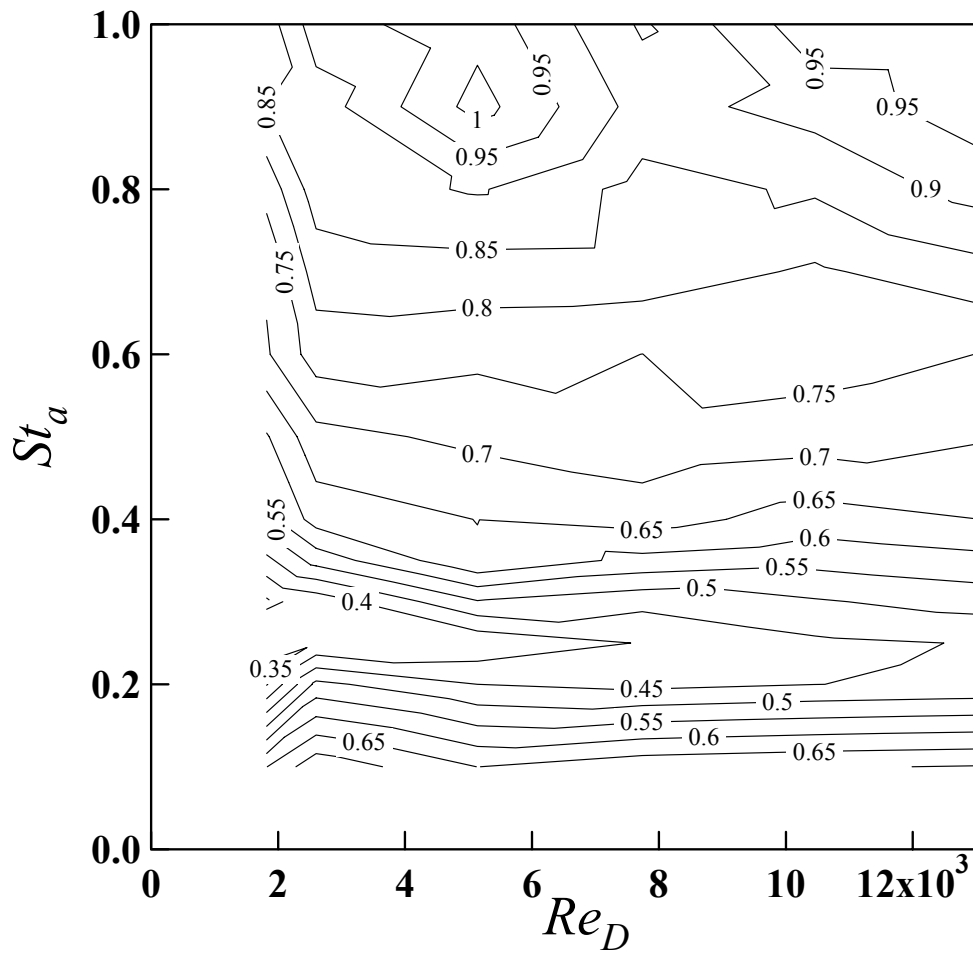


Fig. 12 Relative centerline velocity of the AL controlled jet at various flapping frequencies.

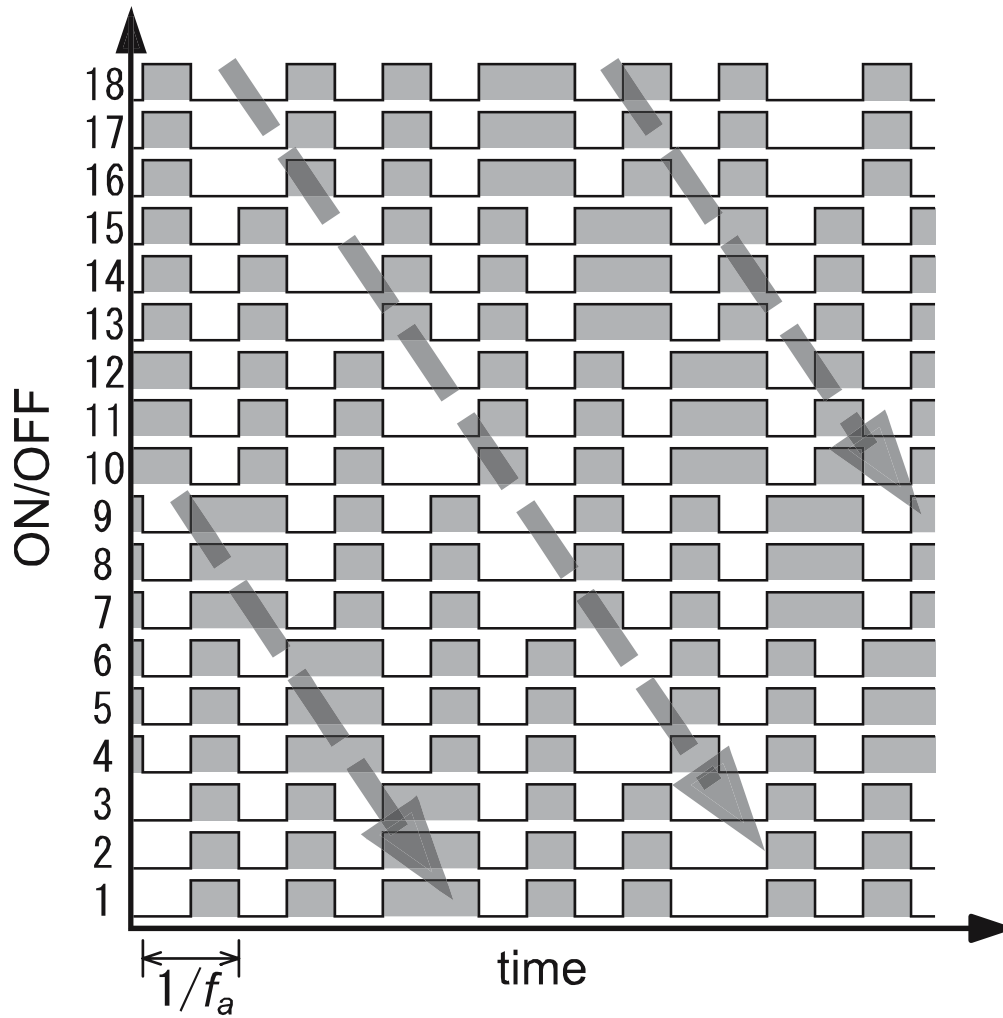


Fig. 13 Control signal diagram of Rotary Alternate Mode.

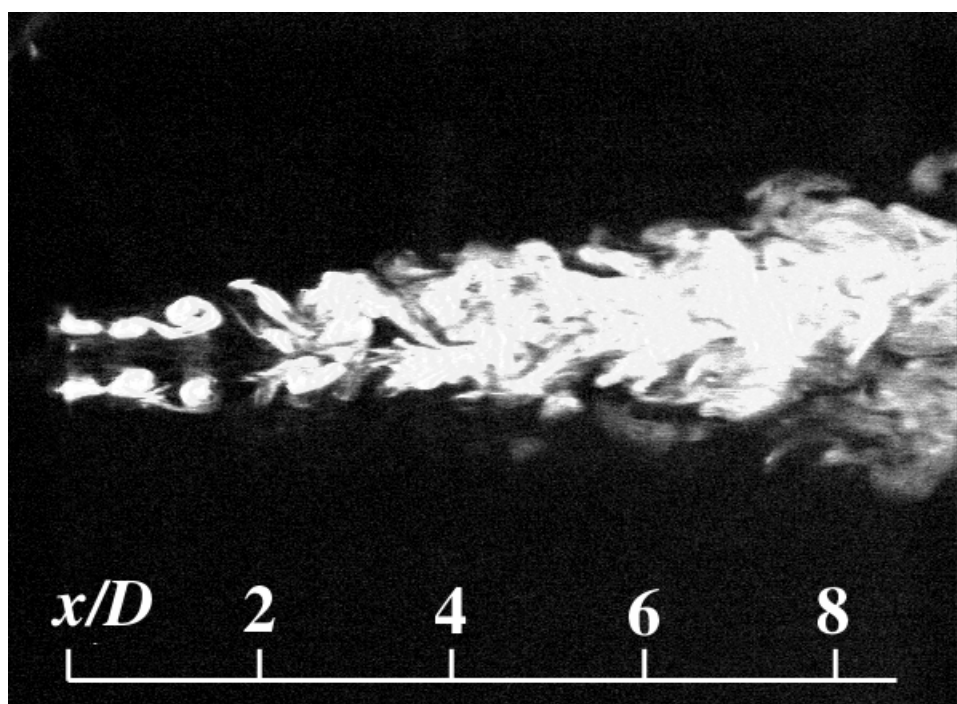


Fig. 14 Longitudinal sectional view of Rotary Alternate Mode.

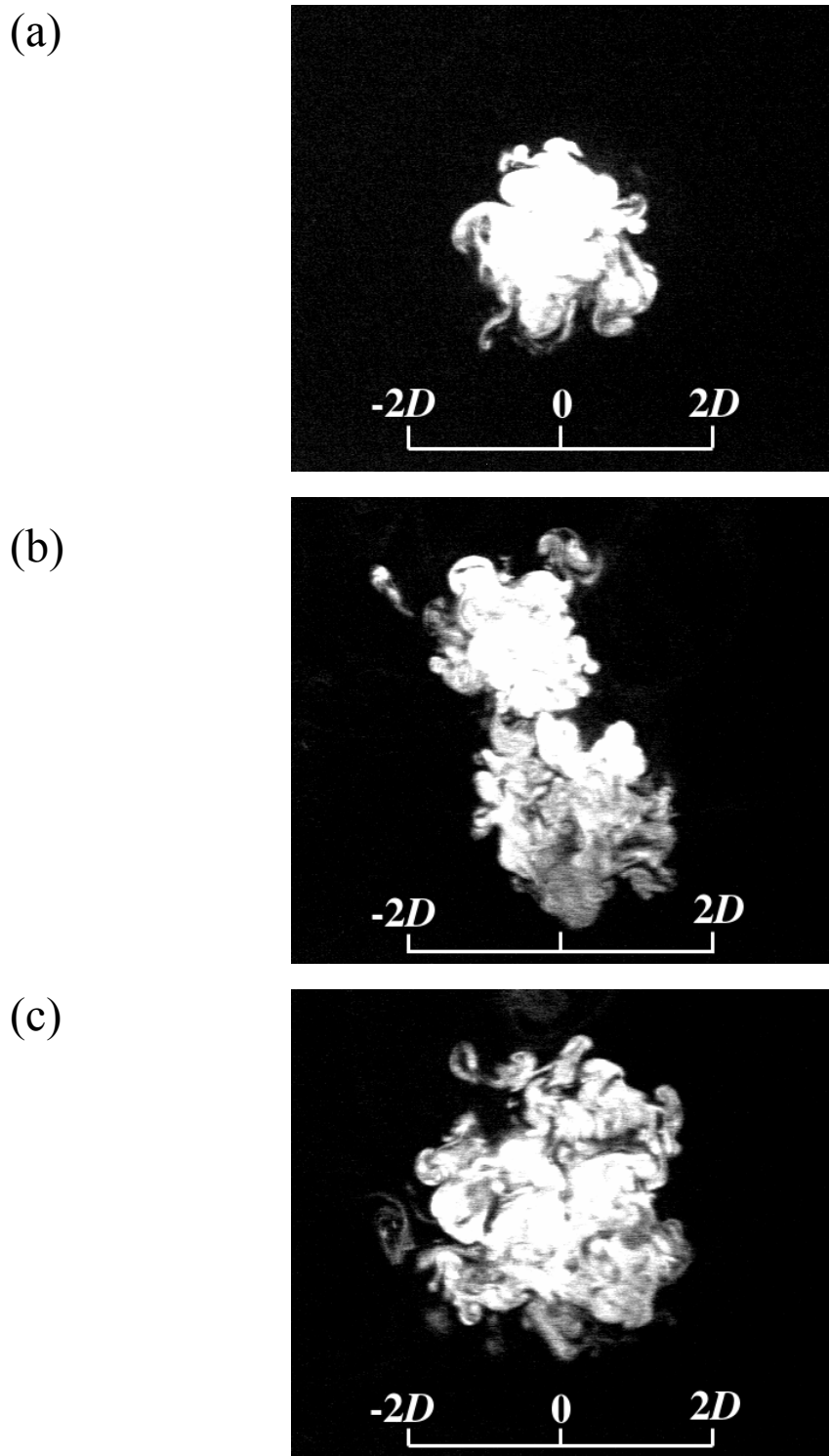


Fig. 15 Transverse sectional views at  $x/D = 8$ ; (a) Natural jet, (b) Alternate Mode, (c) Rotary Alternate Mode.

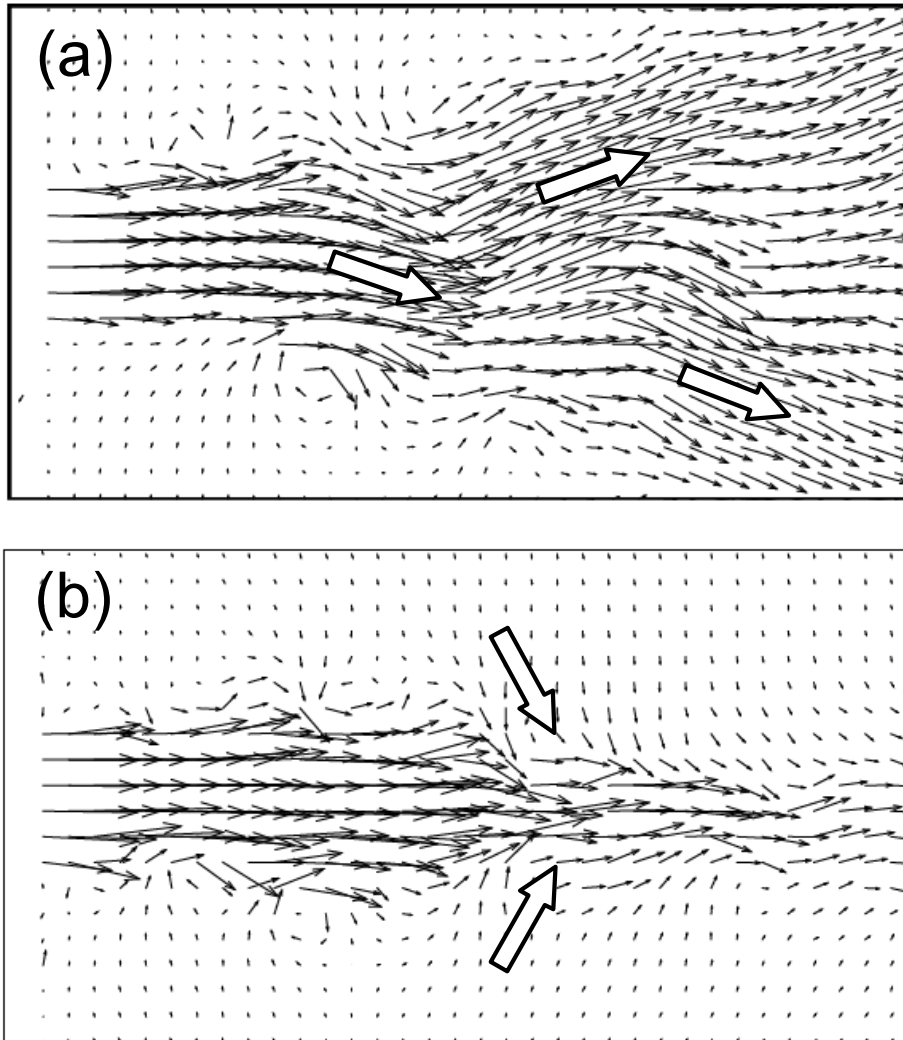


Fig. 16 Phase-averaged velocity vectors for Alternate Mode at  $St_a = 0.25$ . (a) Bifurcating plane, (b) Bisecting plane.

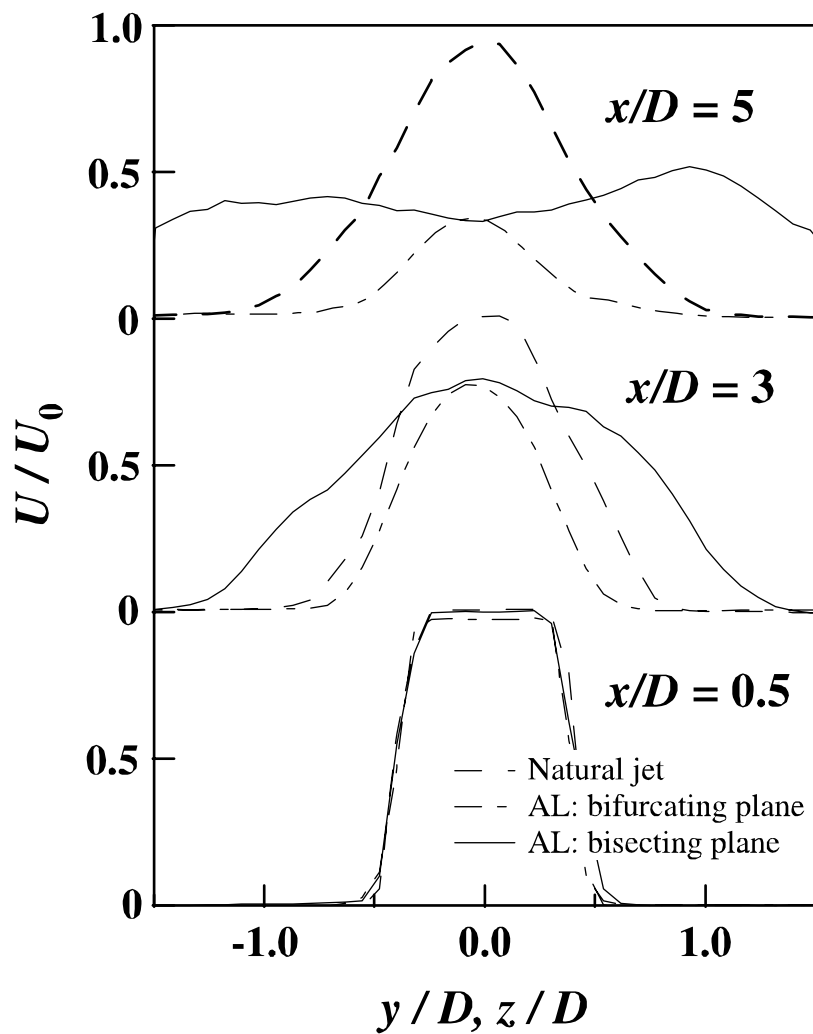


Fig. 17 Cross-stream distributions of streamwise mean velocity.

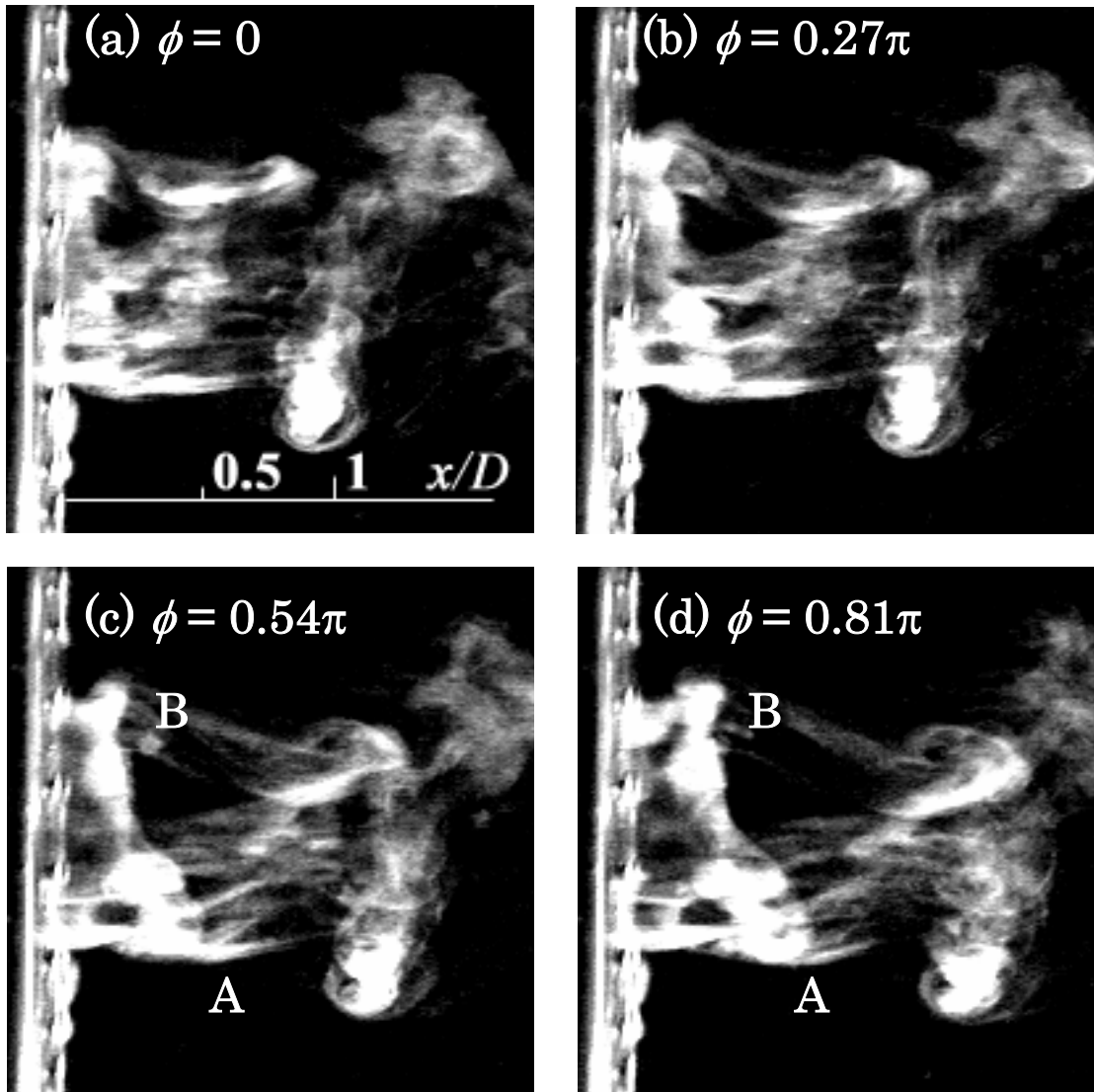


Fig. 18 Successive flow visualization images near the nozzle exit for Alternate Mode at  $St_a = 0.25$ .

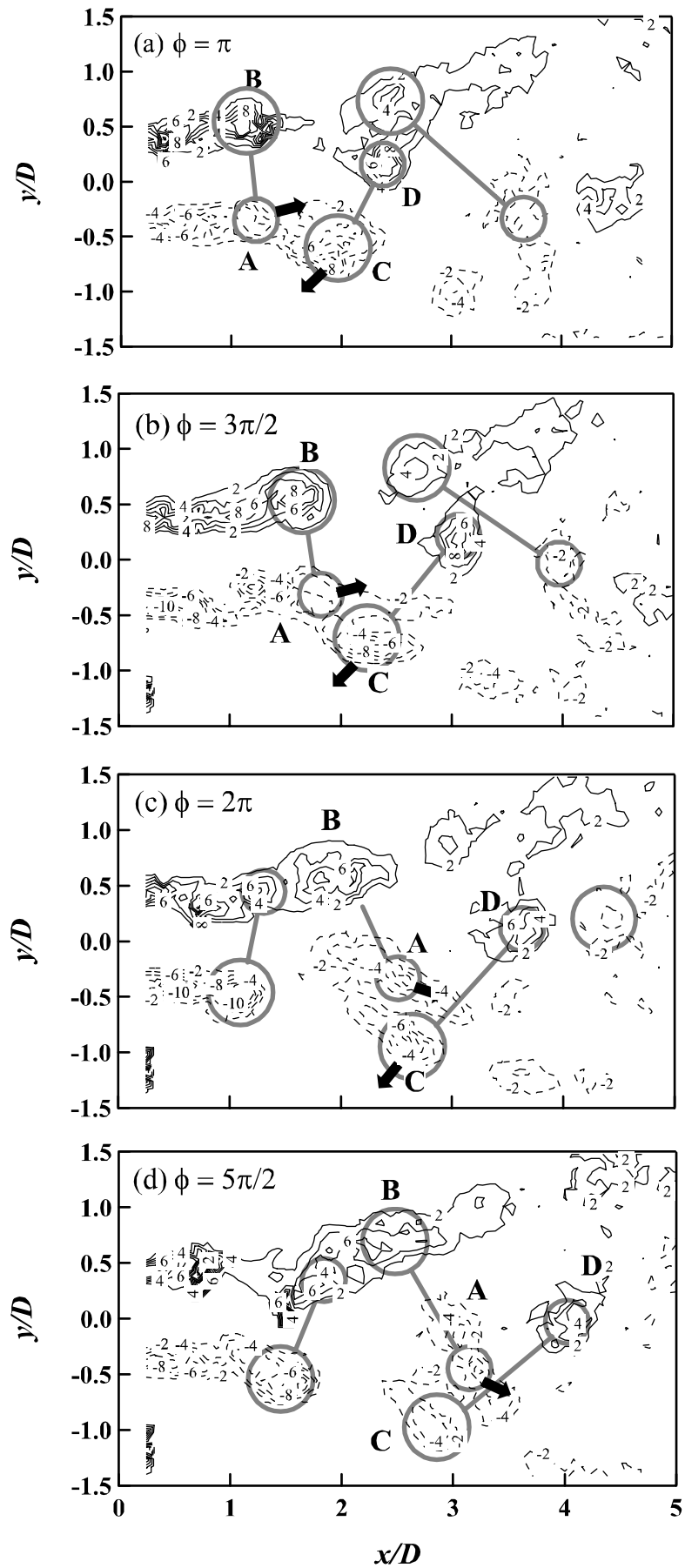


Fig. 19 Successive vorticity contours for Alternate Mode at  $St_a = 0.25$ .



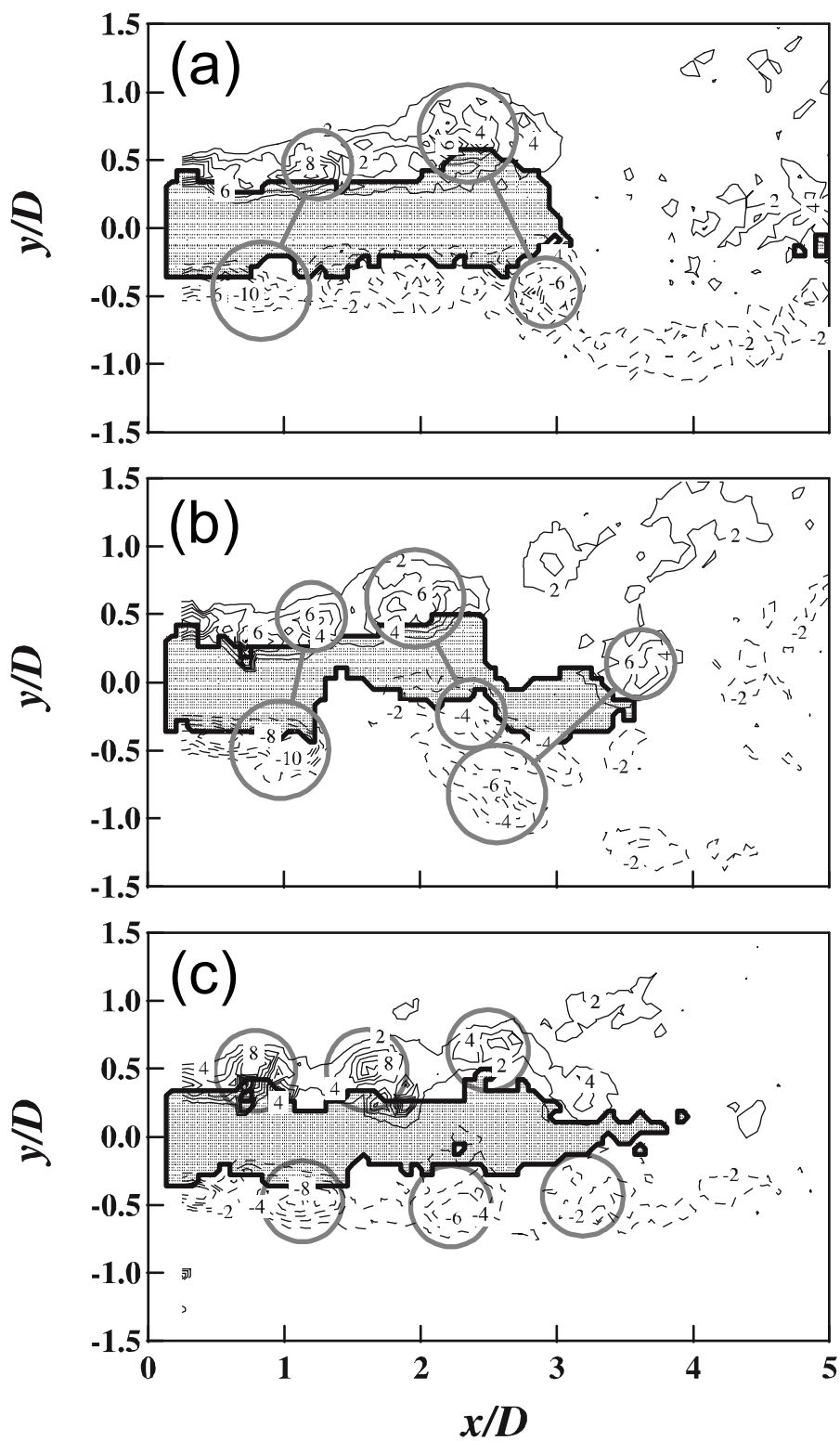


Fig. 20 Jet core ( $\langle U_{abs} \rangle > 0.85U_0$ , shaded area) and vorticity contours at  $St_a =$  (a) 0.125, (b) 0.25, and (c) 0.5.

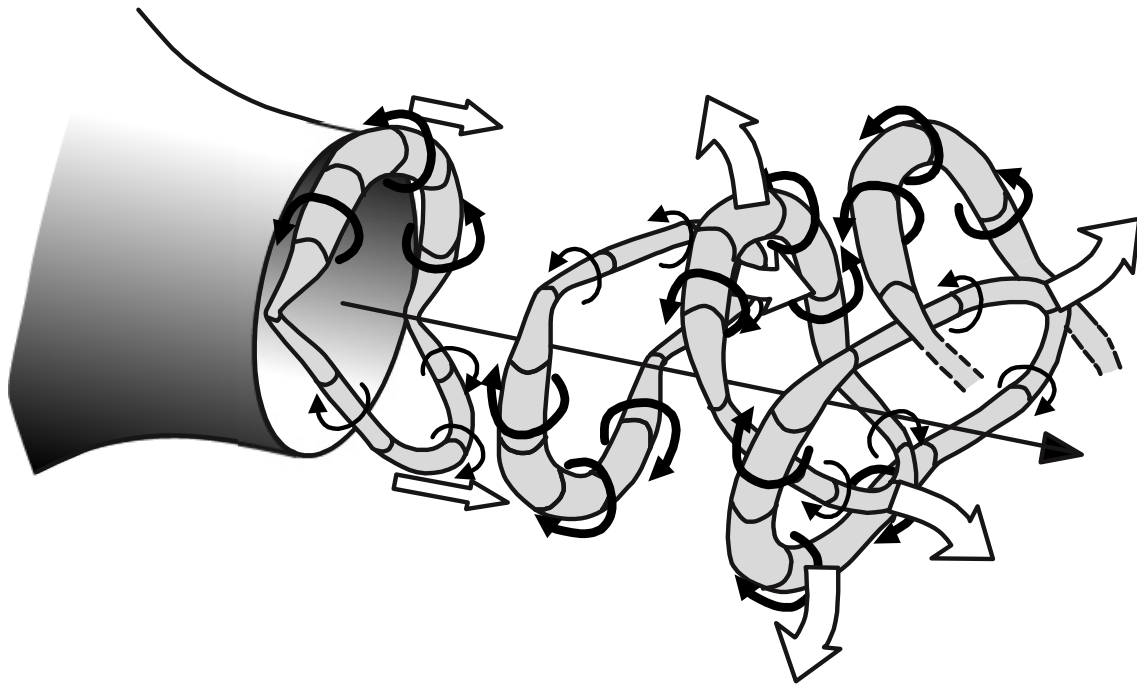


Fig. 21 Proposed model of vortex structures and their motion in the bifurcating jet generated with Alternate Mode.

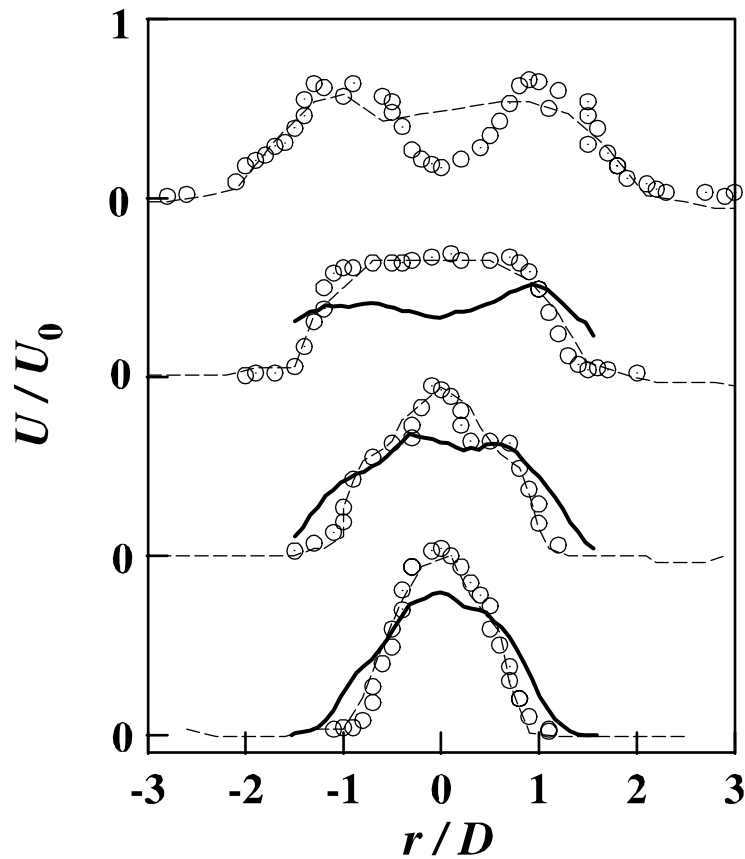


Fig. 22 Comparison of cross-stream distributions of streamwise mean velocity in the bifurcating planes. The solid line represents the present study ( $x/D = 3, 4, \text{ and } 5$ ). The circle data symbols represent data from Lee and Reynolds ( $x/D = 3, 4, 5, \text{ and } 6.5$ ). The broken line represents data from Danaila and Boersma ( $x/D = 3.1, 4.15, 5.2, \text{ and } 6.25$ ).